

Semi-Cosmological Simulations of Baryonic Gas in Growing Dark Matter Halos

A THESIS
SUBMITTED FOR THE DEGREE OF
Master of Science

BY

Shashank Dattathri
Undergraduate Department
Indian Institute of Science

UNDER THE SUPERVISION OF

Prof. Prateek Sharma
Department of Physics
Indian Institute of Science



Indian Institute of Science
Bangalore – 560 012 (INDIA)

June, 2021

Declaration of Originality

I, **Shashank Dattathri**, with SR No. **11-01-06-20-92-20-1-18970** hereby declare that the material presented in the thesis titled

Semi-Cosmological Simulations of Baryonic Gas in a Growing Dark Matter Halo

represents original work carried out by me from **Aug 2020** to **June 2021**.

With my signature, I certify that:

- I have not manipulated any of the data or results.
- I have not committed any plagiarism of intellectual property. I have clearly indicated and referenced the contributions of others.
- I have explicitly acknowledged all collaborative research and discussions.
- I have understood that any false claim will result in severe disciplinary action.
- I have understood that the work may be screened for any form of academic misconduct.

Date: **18/06/2021**



Student Signature

In my capacity as supervisor of the above-mentioned work, I certify that the above statements are true to the best of my knowledge, and I have carried out due diligence to ensure the originality of the report.

Advisor Signature

Prateek Sharma

Associate Professor

Indian Institute of Science

Acknowledgments

First and foremost, I thank my advisor Prof. Prateek Sharma for the constant guidance and encouragement throughout the project. I gained an immense amount of knowledge from working with him, both in astrophysics and the scientific methodology in general. He was always available to meet and discuss about anything I wanted to talk about, and for this I am sincerely grateful.

I also thank the Undergraduate Department, IISc and the Department of Physics, IISc for giving me this opportunity and all the required resources to work on this exciting topic.

I thank Prakriti Pal Choudhury (Institute of Astronomy, University of Cambridge), Prof. Benedikt Diemer (University of Maryland), and Siddhartha Gupta (University of Chicago) for their valuable comments and suggestions.

Finally, I thank my friends and family for their constant support and encouragement throughout my project.

Abstract

In this project, we aim to study the evolution of baryonic gas in a cosmologically growing dark matter halo. We perform the simulations using the astrophysical MHD code PLUTO. We use a dark matter profile that transitions smoothly from the NFW profile within the virial radius to a more realistic profile outside of the virial radius (Diemer and Kravtsov 2014), and we construct the dark matter potential from this density profile. In addition, we introduce a cosmological potential which accounts for an evolution that is consistent with Hubble expansion at all times. Unlike cosmological simulations that use comoving coordinates, we use physical coordinates to solve our equations. We use spherical coordinates and apply an outflow inner boundary condition so that the gas thermalizes via an outward-moving virial shock. Cold gas is initialized with a density which is 0.2 (the universal baryon fraction) times the dark matter density. In the absence of radiative cooling and active galactic nuclei (AGN) feedback, the gas density profiles behave self-similarly across cosmological time for different initial conditions. We study the various mechanisms that govern the formation and evolution of the virial shock and the evolution of the baryon fraction.

We then include the effects of radiative cooling and AGN jet feedback in our model. The feedback is modeled by the accretion of cold gas onto a central supermassive black hole (SMBH). The inner regions of the halo exhibit heating and cooling cycles due to the feedback. The strength and duration of these cycles strongly depend on the efficiency of the AGN feedback and the halo mass. The central SMBH initially grows exponentially with time in the quasar phase of evolution, but the growth slows down at later stages. Our setup is a unique framework that provides a bridge between full cosmological galaxy formation simulations and idealized halo simulations, which will provide greater insight into the evolution of the circumgalactic medium with redshift and halo mass.

Contents

Acknowledgments	i
Abstract	ii
Contents	iii
List of Figures	v
List of Tables	viii
1 Introduction	1
2 Literature Review	3
2.1 Basic Cosmological Background	3
2.2 Gravitational Collapse	4
2.3 Mass Accretion History	5
2.4 Density Profiles of Dark Matter Halos	6
2.5 Radiative Cooling and Metallicity Enrichment	7
2.6 Feedback Mechanisms and SMBH Growth	7
3 Physical Setup	9
3.1 Basic Hydrodynamical Equations	9
3.2 The PLUTO Code	10
3.3 Dark Matter Halo Evolution	10
3.4 Grid, Initial, and Boundary Conditions	11
3.5 Gravitational Potential	12
3.6 Radiative Cooling	14
3.7 Evolution of the Central Supermassive Black Hole	14
3.8 AGN Jet Feedback	16
4 Results	17
4.1 Non-Radiative Runs	17
4.1.1 Hubble Expansion	18
4.1.2 Formation of the Virial Shock	18
4.1.3 Baryon Fraction Evolution	18
4.1.4 Self-Similar Evolution	19
4.2 Maintaining a Constant Baryon Fraction	20
4.3 Runs with Radiative Cooling	21
4.3.1 Lower Mass Halos	22
4.3.2 Higher Mass Halos	23
4.4 Runs with AGN Feedback	26

4.4.1	General Properties	27
4.4.2	Varying the efficiency	29
4.4.3	Varying the Halo Mass	31
4.4.4	Varying the Seed Black Hole Mass	31
4.4.5	Baryon Fraction Evolution	33
5	Conclusions	35
	References	37

List of Figures

3.1	Mass accretion histories of dark matter halos with the $z = 0$ mass ranging from 10^{11} to $10^{15}M_{\odot}$. These growth histories are calculated according to [3], using the parameters $\Omega_m = 0.27$, $h = 0.7$, $\sigma_8 = 0.82$, and $n_s = 0.95$. We note that more massive halos grow faster than less massive ones and therefore have larger values of $z_{0.04}$, the redshift when they reach 4% of the mass at $z = 0$ (see equation 3.12).	11
3.2	Gravitational potential, acceleration, density, and the local density power law index ($d \ln \rho / d \ln r$) as a function of radius given by equations 3.18 and 3.19. The halo mass is $M_0 = 10^{14}M_{\odot}$ and the concentration parameter c is set to 4.	13
3.3	The cooling function (see Eq. 3.26) that we implement for various metallicities, as described by [44]. The value of Λ is strongly dependent on the metallicity, which suggests that the metallicity evolution of the ICM and the IGM plays an important role for gas cooling within halos.	15
4.1	Density, pressure, velocity, and temperature profiles for the non-radiative runs with $M_0 = 10^{14}M_{\odot}$. The inner halo ($< 10^{-2}R_{200c}$) gas shows a core, with a nearly constant temperature and density. The gas at the outer radii $> 10R_{200c}$ are driven by Hubble expansion, with velocity linearly increasing with radius as $v = H(z)r$. This adiabatic expansion leads to a low temperature in the outer regions.	17
4.2	Plot of $v_{out}/(H(z)r_{out})$ (outer radial velocity scaling with time-dependent Hubble expansion) as a function of time for $M_0 = 10^{14}M_{\odot}$. Note that the outer velocity closely follows Hubble expansion due to the cosmological potential (equation 3.24).	18
4.3	Formation of the virial shock for $M_0 = 10^{14}M_{\odot}$ as seen in this pressure versus radius plot at early times. We can see that the shock is not stationary at early times, and slowly transitions to a localized shock near R_{200c} .	19
4.4	Baryon fraction as a function of radius for $M_0 = 10^{14}M_{\odot}$ for non-evolving DK14 parameters $s_e = 1.5$ and $b_e = 1.5$. This choice of parameters result in a baryon fraction that is lesser than the universal value within the virial radius at all times.	19
4.5	Density (ρ) versus scaled radius (r/R_{200c}) for different halo masses at $z=1$ (left panel) and $z=0$ (right panel). In the absence of radiative cooling and feedback, the density profiles are reasonably self-similar with respect to the halo mass at all times after the initial transients.	20
4.6	Baryon fraction evolution for a non-radiative run with $M_0 = 10^{14}M_{\odot}$, using the redshift-dependent parameters for s_e and b_e listed in table 4.2. Using these values, the baryon fraction at the virial radius is close to the universal value at all times. As the parameters s_e and b_e characterize the outer profile, the inner radii ($r < 10^{-1}R_{200c}$) are unaffected by this change in parameters.	22
4.7	Cooling flow profiles for $M_0 = 10^{12}M_{\odot}$. The gas quickly cools to the floor temperature and no virial shock is formed.	22
4.8	t_{cool}/t_{ff} vs r for $M_0 = 10^{12}M_{\odot}$ with radiative cooling. The values are small at all times after the initial transients, which correspond to a strong cooling flow.	23

4.9	Cooling flow profiles for $M_0 = 10^{14}M_\odot$. For this halo mass, the radiative cooling strongly affects the inner regions, as the density profile is cuspy instead of core-like and the temperature decreases compared to the non-radiative runs (figure 4.1). However, the regions $> 10^{-1}R_{200c}$ behave very similar to the non-radiative runs, and a stable virial shock is still formed.	24
4.10	The ratio of the cooling time to the free-fall time ($t_{\text{cool}}/t_{\text{ff}}$) versus radius for $M_0 = 10^{14}M_\odot$ with radiative cooling. This quantitatively illustrates that only the innermost regions are subject to a strong cooling flow, while the outer regions have a high value of $t_{\text{cool}}/t_{\text{ff}}$ and are mostly unaffected by cooling.	24
4.11	Formation of virial shock for a cooling flow run with $M_0 = 10^{14}M_\odot$	25
4.12	Baryon fraction evolution for a cooling flow run with $M_0 = 10^{14}M_\odot$, using the same time-dependent parameters in table 4.2. The regions near the virial radius have a baryon fraction close to the universal value, similar to the non-radiative case. The inner regions have much higher baryon fractions, due to the formation of a density cusp in the presence of cooling.	25
4.13	Mass infall rate and mass accretion rate for cooling flow run with $M_0 = 10^{14}M_\odot$	26
4.14	Mass of the central SMBH over time for cooling flow run with $M_0 = 10^{14}M_\odot$. The mass of the black holes at $z = 0$ differ by a factor of $\approx 10^2$, which is the same as the difference in mass transport efficiencies ϵ_m . Even though the accretion rate is limited by the Eddington limit at early times, the later stages of evolution mostly depend on the efficiency of mass transport to the event horizon.	27
4.15	Snapshots of the density (left) and temperature (right) for $M_0 = 10^{14}M_\odot$ and $\epsilon_m = 10^{-4}$	28
4.16	Normalized quantities \dot{M}_{acc} , $M_{\text{cold}}(< 5\text{kpc})$, jet power (calculated by the method described in section 4.4), and $\min(t_{\text{cool}}/t_{\text{ff}})$ for $M_0 = 10^{14}M_\odot$, $\epsilon_m = 10^{-4}$, and $M_{\text{BH},0} = 10^6M_\odot$. The data is sampled every ~ 10 Myr. The spikes in jet power are mostly associated with increase in $\min(t_{\text{cool}}/t_{\text{ff}})$, increase in black hole accretion rate, and decrease in cold gas mass within 5 kpc, indicating heating and uplifting of gas by the AGN jets.	29
4.17	Same quantities as figure 4.16 for different efficiencies and halo masses. It is clear that feedback runs with a larger efficiency are characterized by greater jet power, larger values of $\min(t_{\text{cool}}/t_{\text{ff}})$, and longer heating/cooling cycles, indicating that more gas is expelled from the core. Smaller halo masses also show similar results.	30
4.18	Variation of the time-averaged mass inflow rate at ~ 1 kpc with efficiency (left panel) and halo mass (right panel), normalized to the corresponding cooling flow run for each halo. Left: average \dot{M}_{in} vs total efficiency ϵ for different halo masses. Right: average \dot{M}_{in} vs M_0 for different values of ϵ . It is clear that the inflow rate at \dot{M}_{in} is more suppressed for greater efficiency as well as lower halo masses.	31
4.19	Variation of the SMBH accretion rate \dot{M}_{acc} with efficiency. The accretion rate is defined as $\min(\epsilon_m \dot{M}_{\text{in}}, \dot{M}_{\text{Edd}})$. We can see from the figure that the accretion rate increases with increase in efficiency, as opposed to the inflow rate \dot{M}_{in} . The decrease in inflow rate due to the heating and expulsion of gas from the AGN jets is more than compensated by the increase in the fraction of mass that is transported to the black hole event horizon.	32
4.20	Value of $\dot{M}_{\text{acc}}/\dot{M}_{\text{Edd}}$ over time for different seed black hole masses and efficiencies. The runs with a smaller seed black hole mass have a longer initial time period where $\dot{M}_{\text{acc}} \sim \dot{M}_{\text{Edd}}$, ranging from ~ 200 Myr for $M_{\text{BH},0} = 10^4M_\odot$ to only a few Myr for $M_{\text{BH},0} = 10^7M_\odot$	32
4.21	Growth of the central SMBH for different seed black hole masses and efficiencies. The black holes grow exponentially with time in the initial quasar stage of evolution (corresponding to the linear portion of the semilog graph). It is clear that after the initial growth phase, the value of $M_{\text{BH},0}$ is largely independent of the initial mass, and the value of ϵ_m plays a much more important role in the evolution at later stages.	33

4.22	Normalized baryon fraction evolution for $M_0 = 10^{14} M_\odot$, with AGN feedback efficiency $\epsilon = 10^{-5}$ and redshift-dependent DK14 parameters (table 4.2). Similar to the effect of radiative cooling, the effects of AGN feedback are prominent only in the inner radii of the halo. The baryon fraction within $10^{-2} R_{200c}$ is very low because the AGN jets cause bubbles with hot, low density gas. The baryon fraction beyond the virial radius reaches the universal value, similar to the non-radiative and cooling flow runs.	34
------	---	----

List of Tables

4.1	Results of the non-radiative runs. The core temperature and the virial temperature (temperature at R_{200c}) both increase with halo mass.	21
4.2	DK14 parameters for different halo masses for maintaining universal baryon fraction.	21
4.3	Mass of the black hole at various stages of the AGN evolution.	33

Chapter 1

Introduction

According to the standard Λ CDM (Λ cold dark matter) paradigm of structure formation in the Universe, the dynamical evolution of galaxy clusters is primarily governed by dark matter halo dynamics. Whereas, in addition to following the dark matter gravity, the gas (which constitutes $\sim 80\%$ of baryons within massive halos) is strongly affected by radiative cooling and feedback powered by accretion onto a central supermassive black hole. Cosmological N-body simulations provide a good description for the large-scale (on scales larger than the halo) distribution of baryonic and dark matter in the Universe. However, the evolution of baryons within individual halos is more complex and requires including processes such as radiative cooling and feedback heating. Recent state-of-the-art simulations like IllustrisTNG [39] include baryonic physics, but the resolution is not sufficient to study feedback processes in detail. Most of the idealized simulations of baryonic processes in isolated halos assume a static dark matter halo (e.g. [29], [11]), and various important parameters (such as the metallicity of the IGM, e.g. [4]) are not evolved cosmologically.

The standard spherical infall model of gas inside dark matter halos predicts a density profile $\rho \propto r^{-2} - r^{-3}$. This is in general agreement with N body simulations. The density profile of dark matter within halos in N-body cosmological simulations is well described by the NFW (Navarro-Frenk-White) profile ([25]). However, the outer regions of the halo do not follow the NFW profile as the density cannot continuously decrease with radius and must match the average density of the Universe far away from the halo. [9] study the dependence of the outer density profile of a halo on its mass accretion rate and give a more realistic profile that applies outside of the virial radius. Thus, in order to study the evolution of galaxy clusters beyond the virial radius, it is necessary to accurately model both the inner and outer regions of the halo.

In the absence of radiative cooling and feedback heating, the gas is expected to follow the dark matter profile and behave self-similarly with respect to the virial mass. The gas within the halo thermalizes via an outward moving pressure-supported virial shock [1]. The innermost regions of the halo form a core with a nearly constant density and temperature. The gas evolution closely follows the dark matter evolution [4], leading to a baryon fraction within the virial radius that is nearly equal to the universal value of $1/6$ [38].

However, the hot gas profiles as measured by X-ray observations are not self-similar in groups and clusters. Since cooling efficiency of hot gas depends strongly on the temperature, radiative cooling is expected to break self-similarity in baryons. The cooling time in the inner regions of the halo is short, which in absence of heating, would lead to catastrophic cooling and intense star formation. This cooling flow model predicts a gas inflow rate of $100 - 1000 M_{\odot} yr^{-1}$, which is at least an order of magnitude greater than what we observe. Thus, some source(s) of heating is required in order to prevent catastrophic cooling.

A promising heating mechanism is feedback due to active galactic nuclei (AGN) powered by accretion onto the central supermassive black hole. Several observational studies by Chandra and XMM-Newton have shown the presence of jet-driven X-ray cavities and bubbles. Numerical studies of AGN feedback have shown that an efficiency $\gtrsim 10^{-4}$ ($\dot{E}_{jet} = 10^{-4} \dot{M}_{in} c^2$) is enough to suppress the inflow rate in galaxy clusters by a factor of ~ 10 [29] compared to a cooling flow. The accretion rate onto the black hole depends on this mass inflow rate, the efficiency of mass transport to the event horizon, and is limited by the Eddington rate. The evolution of the

central supermassive black hole is characterized by an initial phase where the accretion rate is high (termed as the quasar regime) and a later phase where the accretion rate is low (the radio regime) [37]. This has important implications for the growth of supermassive black holes which power AGN [5].

In this work, we study the evolution of baryonic gas in a cosmologically evolving dark matter halo. We evolve the dark matter halo mass and density profiles, the metallicity of the intergalactic medium (IGM), and the mass of the central supermassive black hole across cosmological time. However, the regions beyond the halo evolve according to Hubble expansion. Our model is therefore self-consistent with various aspects of cosmological evolution and structure formation.

This thesis is organized as follows. In chapter 2, we review some basic concepts of cosmology and structure formation, as well as some of the recent works in this field. In chapter 3, we describe our semi-cosmological setup for studying the baryonic gas in an evolving halo. We describe the results of our simulations in chapter 4 and their implications. Finally, we conclude in chapter 5.

Chapter 2

Literature Review

2.1 Basic Cosmological Background

The metric of a homogeneous and isotropic three-dimensional hypersurface can be written as [43]

$$dl^2 = a^2(t) \left[\frac{dr^2}{1 - Kr^2} + r^2(d\nu^2 + \sin^2 \nu d\phi^2) \right] . \quad (2.1)$$

where $a(t)$ is the time-dependent scale factor and K is a constant which can take the values -1 , 0 , and $+1$. These describe the space-like hypersurfaces corresponding to a constant cosmic time t . The metric of the four-dimensional space-time can be therefore written as

$$ds^2 = c^2 dt^2 - dl^2 = c^2 dt^2 - a^2(t) \left[\frac{dr^2}{1 - Kr^2} + r^2(d\nu^2 + \sin^2 \nu d\phi^2) \right] , \quad (2.2)$$

which is known as the Robertson-Walker metric.

The proper distance d and the comoving distance d_c are related in this metric by

$$d = a d_c . \quad (2.3)$$

The Hubble parameter $H(t)$ is defined as

$$H(t) = \frac{\dot{a}(t)}{a(t)} , \quad (2.4)$$

and its value at the present time is denoted by H_0 . It is also convenient to define

$$h = \frac{H_0}{100 \text{ km s}^{-1} \text{ Mpc}^{-1}} . \quad (2.5)$$

The redshift parameter at a time t is defined as

$$1 + z = \frac{a(t_0)}{a(t)} . \quad (2.6)$$

According to the standard model of cosmology, the space-time geometry is described by the Einstein field equation in terms of the matter/energy content in the universe:

$$R_{\mu\nu} - \frac{1}{2} g_{\mu\nu} R - g_{\mu\nu} \Lambda = \frac{8\pi G}{c^4} T_{\mu\nu} , \quad (2.7)$$

where $R_{\mu\nu}$ is the Ricci tensor, R is the curvature scalar, $g_{\mu\nu}$ is the metric tensor, and $T_{\mu\nu}$ is the energy-momentum tensor. For a homogeneous and isotropic universe, the metric tensor is given by the Robertson-Walker metric.

We then have

$$\left(\frac{\dot{a}}{a}\right)^2 = \frac{8\pi G}{3}\rho - \frac{Kc^2}{a^2} + \frac{\Lambda c^2}{3}, \quad (2.8)$$

which is known as the Friedmann equation. This cosmology is called the Friedmann-Robertson-Walker (FRW) cosmology.

The various energy densities of different components of the universe evolve differently in the FRW cosmology:

$$\begin{aligned} \text{matter: } \rho_m &\propto a^{-3}, \\ \text{radiation: } \rho_r &\propto a^{-4}, \\ \text{vacuum energy: } \rho_\Lambda &\propto a^0. \end{aligned} \quad (2.9)$$

The Friedmann equation can then be written as

$$\left(\frac{\dot{a}}{a}\right)^2 = H^2(t) = \frac{8\pi G}{3} \left[\rho_{m,0} \left(\frac{a_0}{a}\right)^3 + \rho_{r,0} \left(\frac{a_0}{a}\right)^4 + \rho_{\Lambda,0} \right] - \frac{Kc^2}{a^2}. \quad (2.10)$$

The quantities $\rho_{m,0}$, $\rho_{r,0}$, and $\rho_{\Lambda,0}$ can be determined by theoretical and observational considerations. The mass density is

$$\rho_{m,0} = \Omega_{m,0} \rho_{crit,0} \approx 1.88 \times 10^{-29} \Omega_{m,0} h^2 \text{g cm}^{-3}, \quad (2.11)$$

where

$$\rho_{crit}(t) = \frac{3H(t)}{8\pi G} \quad (2.12)$$

is the critical density at time t , and the subscript 0 denotes the present time. The current observations give [38]

$$\Omega_{m,0} = 0.27 \pm 0.05 \quad h = 0.72 \pm 0.05. \quad (2.13)$$

The redshift evolution of the Hubble parameter $H(z)$ is given by

$$H(z) = H_0 E(z), \quad (2.14)$$

where

$$E(z) = [\Omega_{\Lambda,0} + \Omega_{m,0}(1+z)^3 + \Omega_{r,0}(1+z)^4 + (1 - \Omega_{\Lambda,0} - \Omega_{m,0} - \Omega_{r,0})(1+z)^2]. \quad (2.15)$$

This can be used to determine the redshift evolution of the Ω parameters:

$$\Omega_\Lambda = \frac{\Omega_{\Lambda,0}}{E^2(z)} \quad \Omega_m = \frac{\Omega_{m,0}(1+z)^3}{E^2(z)}. \quad (2.16)$$

For a flat universe, $\Omega_{m,0} + \Omega_{\Lambda,0} = 1$. In this case, the lookback time as a function of redshift can be written in a closed form: [14]

$$t(z) = \frac{1}{H_0} \frac{2}{3\sqrt{\Omega_{\Lambda,0}}} \ln \left[\frac{\sqrt{\Omega_{\Lambda,0}(1+z)^{-3}} + \sqrt{\Omega_{\Lambda,0}(1+z)^{-3} + \Omega_{m,0}}}{\sqrt{\Omega_{m,0}}} \right]. \quad (2.17)$$

2.2 Gravitational Collapse

A perturbation in the cosmic density field evolves hierarchically, according to the gravitational spherical collapse model. We consider an initial overdensity given by

$$\rho(\mathbf{x}, t) = \bar{\rho}(t)[1 + \delta(\mathbf{x}, t)]. \quad (2.18)$$

According to the linear perturbation theory, in the linear regime the growing mode of the perturbation evolves as

$$\delta_+ \propto D(z) \propto g(z)/(1+z), \quad (2.19)$$

where $D(z)$ is called the linear growth rate, and $g(z) \approx \frac{5}{2}\Omega_m(z) \left[\Omega_m^{4/7}(z) - \Omega_\Lambda(z) + [1 + \Omega_m(z)/2][1 + \Omega_\Lambda(z)/70] \right]^{-1}$. The critical overdensity for collapse is given by [14]

$$\delta_c \approx \begin{cases} 1.686[\Omega(t_{col})]^{0.0185} & \Lambda = 0, \\ 1.686[\Omega_m(t_{col})]^{0.0055} & \Lambda \neq 0. \end{cases} \quad (2.20)$$

Both cases have a very weak dependence on Ω and Ω_m , so we can take $\delta_c \approx 1.686$ for all cosmologies.

The Press-Schechter formalism [31] tells that the probability that $\delta_s > \delta_c(t)$ is the same as the fraction of mass elements that are contained in halos with mass greater than M at any point t . If we consider a Gaussian distribution for the initial overdensity, the number density of halos evolves as

$$n(M, t)dM = \sqrt{\frac{2}{\pi}} \frac{\bar{\rho}}{M^2} \frac{\delta_c}{\sigma} \exp\left(-\frac{\delta_c^2}{2\sigma^2}\right) \left| \frac{d \ln \sigma}{d \ln M} \right| dM, \quad (2.21)$$

where $\sigma(M)$ is the variance of the matter power spectrum. This tells us that halos of mass M are formed in significant number only when $\sigma(M) > \delta_c(t)$. A characteristic mass of M^* can therefore be defined as

$$\sigma(M^*) = \delta_c/D(t), \quad (2.22)$$

where $D(t)$ is the linear growth rate at time t . As $D(t)$ increases with time, the value of M^* increases, implying that more massive halos are formed in significant number only at later times.

2.3 Mass Accretion History

It is clear from the above discussion that dark matter halos grow hierarchically, through the accretion of matter onto the halo from the surrounding medium and the merger with other halos. Since this growth is a highly non-linear process, semi-analytical models of the formation and evolution of dark matter halos is usually based on cosmological N-body simulations. The Press-Schechter (PS) formalism and the extended Press-Schechter (EPS) formalism provide an explanation for the mass accretion histories of halos of a wide range of masses and cosmologies. The mass history of an individual halo can be represented conveniently in the form of a merger tree, which yields the masses of the progenitors of the main halo. A summary of the different merger tree-based methods for analyzing the evolution of dark matter halo evolution is given in [17].

For our work, we are not concerned about the detailed distribution of the masses of the progenitor halos or the exact rate of mergers. Rather, we wish to focus on the mass of the main halo as a function of time. Van den Bosch (2002) [41] use the EPS formalism to construct the mass accretion histories of a wide range of halos in various cosmologies. They found that the average accretion history of a halo follows a two-parameter universal form:

$$\log(M(z)/M_0) = -0.301 \left[\frac{\log(1+z)}{\log(1+z_f)} \right]^\nu, \quad (2.23)$$

where z_f and ν are fitting parameters. Here, M_0 is the mass of the halo at the present redshift, and z_f is the formation redshift of the halo, defined as $M(z_f) = M_0/2$. Similar models of average halo mass growth have been examined by several others ([21], [6], [7]).

A follow up study by Van den Bosch et al (2014) [3] have found that the halo's maximum circular velocity is a better regulator of galaxy formation than the halo mass. This V_{max} is directly related to the depth of the central potential well. They used merger trees constructed based on the EPS formalism to analyze the potential well growth history (PWGH) of CDM halos. They construct a universal model for the mean and median mass accretion history of a wide range of halos of different masses and cosmologies that are in fair agreement with previous works.

Diemer and Kravtsov 2014 [9] analyzed the evolution of Λ CDM halos, focusing on the effect of the mass accretion rate on the self-similarity of the density profiles and their effect on the outer profiles. They found that the halo peak height $\nu = \delta_c/\sigma(M, z)$ (a measure of the fluctuation over the background cosmic density field corresponding to the halo) is an important parameter that is directly related to the virial mass of halos as a function of redshift. The self-similarity of halos of a large range of masses is evidently sensitive to the overall accretion history (rather than just major mergers). The accretion history also determines the profile of the halo near and outside of the virial radius.

2.4 Density Profiles of Dark Matter Halos

The self-similar model of spherical gravitational collapse tells us that in the Λ CDM cosmology, a density profile follows close to an isothermal sphere $\rho \propto r^{-2}$ at all relevant length scales. However, cosmological simulations show a shallower profile in the inner regions and a steeper profile in the outer regions. Based on several results, the NFW profile was postulated [25]:

$$\rho(r) = \rho_c \frac{\delta_{char}}{(r/r_s)(1 + r/r_s)}, \quad (2.24)$$

where δ_{char} is a characteristic overdensity, usually taken to be 200. We note that the total mass enclosed by the halo tends to ∞ as $r \rightarrow \infty$. It is therefore motivated to choose a radius r_h as the boundary of the halo. The most commonly used definition is the radius where the density is 200 times the mean density, i.e. $\rho(R_{200}) = 200\bar{\rho}$. It is also common to define it with respect to the critical density, i.e. $\rho(R_{200c}) = 200\rho_c$.

The scale radius r_s is related to R_{200} by the concentration parameter c as $r_s = R_{200}/c$. The concentration parameter is directly related to the merger and accretion history of the halo. A halo which recently experienced a major merger would have greater mass and size of the halo in the outer region, thus increasing R_{200} without increasing r_s and a greater value of c . A simple expression for the mean concentration parameter as a function of time and halo mass is given by [47]

$$c(M, t) = 4 \times \left(1 + \left[\frac{t}{3.75t_{0.04}} \right]^{8.4} \right)^{1/8}, \quad (2.25)$$

where $t_{0.04}$ is the time at which the main progenitor of the halo gained 4% of its current mass.

While the NFW profile accurately models a large number of dark matter halos, observations show that there are small (but systematic) deviations. A more accurate is given by the Einasto profile [16]

$$\rho(r) = \rho_{-2} \exp \left[\frac{-2}{\alpha} \left(\left(\frac{r}{r_{-2}} \right)^\alpha - 1 \right) \right], \quad (2.26)$$

where r_{-2} is the radius at which the slope of the profile is -2 , and $\rho_{-2} = \rho(r_{-2})$. The slope of the density profile is given by

$$\frac{d \ln \rho}{d \ln r} = -2 \left(\frac{r}{r_{-2}} \right)^\alpha. \quad (2.27)$$

The Einasto profile has a density slope that is shallower than the NFW profile at small radii. A significant advantage of the Einasto profile over the NFW profile is that the total mass within the halo is finite. Therefore, it eliminates the necessity to arbitrarily introduce a cutoff radius. In addition, the Einasto profile has three free parameters (α , ρ_{-2} , and r_{-2}) and can therefore provide a better fit to data than the NFW profile, which has two free parameters (r_s and δ_{char}).

In both the NFW and the Einasto profile, the density monotonically decreases with radius. In reality, as we go far away from the halo, the density should approach $\bar{\rho}$, the mean density of the universe. Using cosmological N-body simulations, Diemer & Kravtsov [9] (hereafter DK14) introduced a new profile that provides a good

approximation even at large radii

$$\begin{aligned}
\rho(r) &= \rho_{\text{inner}} \times f_{\text{trans}} + \rho_{\text{outer}} , \\
\rho_{\text{inner}} &= \rho_{\text{Einasto}} , \\
\rho_{\text{outer}} &= \bar{\rho} \left[b_e \left(\frac{r}{5R_{200}} \right)^{-s_e} + 1 \right] , \\
f_{\text{trans}} &= \left[1 + \left(\frac{r}{r_t} \right)^\beta \right]^{-\frac{\gamma}{\beta}} .
\end{aligned} \tag{2.28}$$

The outer density profile has two free parameters: b_e and s_e . These parameters are strongly dependent on the mass accretion rate and the peak height ν of the halo.

2.5 Radiative Cooling and Metallicity Enrichment

The cooling of gas and plasma and the mechanical energy injection by AGN jets and supernovae plays an important role in various astrophysical phenomena. The cooling rate depends on a number of factors. The cooling rate is typically dominated by collisional processes, and can be expressed as

$$\mathcal{L} = n_e n_i \Lambda \tag{2.29}$$

where n_e and n_i are the electron and ion densities respectively, and $\Lambda(T, Z)$ is the cooling function. The value of Λ is examined by several authors ([44], [42], [34]), and it is evident that its value depends on several factors. The strongest dependence is on temperature and metallicity, and shows weaker dependence on the number density of electrons and ions and the presence of a radiation field.

It is common to express the cooling function as a sum of the contributions from hydrogen and helium, and the contributions from all heavier elements.

$$\Lambda = \Lambda_{H,He} + \Lambda_{>He} \tag{2.30}$$

The H-He cooling function dominates in low temperatures ($T < 2 \times 10^5$ K) as well as high temperatures ($T > 2 \times 10^7$ K), whereas the cooling function of the heavier elements (metals) dominates in the intermediate temperature range. Wang et al (2014) [42] included a third term in equation 2.30 Λ_{ee} , which accounts for the electron-electron bremsstrahlung cooling. They found that this becomes important at very high temperatures ($T > 10^9$ K) when the atoms are fully ionized and the electrons become relativistic. However, we do not reach such temperatures in our model and therefore neglect the contribution of Λ_{ee} .

Wiersma et al (2009) [44] analyzed the effect of photoionization on the cooling rates of metal-rich gas. They found that in photoionization equilibrium, the total cooling rate is not proportional to the number density squared, as in collisional ionization equilibrium (CIE). The effect of photoionization can also drastically decrease the value of Λ (figure 6 in [44]).

Clearly, the cooling rate of a gas depends heavily on its metallicity. The chemical enrichment of the intergalactic medium (IGM) has been analyzed by the point of view of hydrodynamical simulations of outflows from star-forming galaxies [26], turbulent diffusion of metals and thermal energy due to adiabatic feedback [36], enrichment through galactic winds [24], and intermediate-mass and massive stars through supernovae and stellar winds [45]. It is clear that by $z \sim 0$, most of the gaseous metals are in the WHIM (warm-hot intergalactic medium) [27]. The WHIM has a relatively high metallicity of $10^{-1}Z_\odot$ which evolves weakly over time. The cold-warm interstellar medium (ISM) and the cold-warm IGM exhibit strong cosmological evolution. The redshift dependence of metallicity in the various components is shown in figure 8 of [45] and figure 5 of [26].

2.6 Feedback Mechanisms and SMBH Growth

The cooling times of a large number of galaxy clusters are lesser than 1 Gyr, much shorter than the Hubble time. In the presence of cooling without any heating, we would expect that galaxy clusters would exhibit catastrophic

cooling in the inner regions and would lead to a very high mass inflow rate of $100 - 1000 M_{\odot}/yr$. This would lead to an extremely large star formation rate. However, observations do not reflect this, and show that the actual star formation rate is at least an order or magnitude smaller than the predictions from cool core models [23]. Therefore, some sources of feedback are required in order to heat the core and prevent runaway cooling.

It is now widely believed that feedback by active galactic nuclei (AGN) is the primary heating source that prevents catastrophic cooling in cluster cores. This is strongly motivated by observations by Chandra and XMM-Newton which have uncovered AGN jet-driven X-ray cavities and bubbles at the center of clusters [2]. Idealized simulations of AGN-driven jets impose global thermal equilibrium in the intracluster medium (ICM). The local thermal instabilities lead to condensation of cold gas from the multiphase ICM only if the ratio of the cooling time to the free-fall time is less than 10, i.e. $t_{cool}/t_{ff} < 10$ [35], [12].

Prasad et al (2015) [29] use hydrodynamical simulations to show that a feedback efficiency of as small as 6×10^{-5} is enough to suppress the mass inflow rate by a factor of 10, preventing catastrophic cooling. They model the AGN feedback by the accretion of cold gas onto the central supermassive black hole (SMBH). This leads to a hysteresis cycle: cool gas falls toward the center that accretes onto the SMBH and powers the jet, the jet heats up the surrounding medium and prevents cooling, and then this will lower the jet power and leads to eventual cooling of the freshly heated gas. Their runs implement radiative cooling with a constant metallicity of $0.3 Z_{\odot}$ and a non-evolving dark matter halo. The frequency of these heating/cooling cycles depends on several parameters, including halo mass and efficiency. The presence of a central BCG can decrease the value of $min(t_{cool}/t_{ff})$ by a factor of 2, increasing the core density and decreasing its entropy [30]. The relative importance of the various heating mechanisms is examined by [46].

The central SMBH itself evolves over time. Sijacki et al (2007) [37] perform cosmological simulations with seed black holes at an early cosmic time and grow them by gas accretion as well as mergers with other black holes. It is evident that the cosmological evolution of black holes occurs in two distinct regimes: a quasar regime with a high accretion rate with a high bolometric luminosity that is close to the Eddington limit, and a radio regime where most of the energy is released mechanically via AGN-driven bubbles. The growth of the SMBH increases its Eddington limit over time, leading to the transition from the quasar regime to the radio regime. Churazov et al (2018) [5] show that an isothermal gas halo with a low feedback efficiency ($\approx 10^{-5}$) can achieve a heating-cooling balance once the black hole reaches the observed $M_{BH} - \sigma$ relation.

Chapter 3

Physical Setup

3.1 Basic Hydrodynamical Equations

We use spherical polar coordinates (r, θ, ϕ) to solve the standard hydrodynamical equations with external gravity due to the halo, radiative cooling, and mass and momentum source terms due to AGN jet feedback. In conservative form, the equations are given by

$$\frac{\partial \rho}{\partial t} + \nabla \cdot (\rho \mathbf{v}) = S_\rho , \quad (3.1)$$

$$\frac{\partial(\rho \mathbf{v})}{\partial t} + \nabla \cdot (\rho \mathbf{v} \mathbf{v}) = -\nabla P - \rho \nabla \Phi + S_\rho \mathbf{v}_{jet} , \quad (3.2)$$

$$\frac{\partial}{\partial t} \left(\frac{\rho v^2}{2} + \frac{P}{\gamma - 1} \right) + \nabla \cdot \left[\left(\frac{\rho v^2}{2} + \frac{\gamma P}{\gamma - 1} \right) \mathbf{v} \right] = S_\rho \left(\mathbf{v}_{jet} \cdot \mathbf{v} - \frac{v^2}{2} \right) + S_e - \rho \mathbf{v} \cdot \nabla \Phi - \mathcal{L}_{cool} . \quad (3.3)$$

The non-conservative form of the above equations are

$$\frac{\partial \mathbf{v}}{\partial t} + (\mathbf{v} \cdot \nabla) \mathbf{v} = \frac{\nabla P}{\rho} - \nabla \Phi + \frac{S_\rho}{\rho} \left(\mathbf{v}_{jet} \cdot \mathbf{v} - \frac{v^2}{2} \right) , \quad (3.4)$$

$$\frac{\partial e}{\partial t} + \nabla \cdot (e \mathbf{v}) = -P \nabla \cdot \mathbf{v} + S_e , \quad (3.5)$$

$$\frac{\partial}{\partial t} \left(\frac{\rho v^2}{2} \right) + \nabla \cdot \left(\frac{\rho v^2}{2} \mathbf{v} \right) = S_\rho \left(\mathbf{v}_{jet} \cdot \mathbf{v} - \frac{v^2}{2} \right) + S_e - \rho \mathbf{v} \cdot \nabla \Phi - \mathbf{v} \cdot \nabla P - \mathcal{L}_{cool} . \quad (3.6)$$

In the above equations, ρ is the mass density, \mathbf{v} is the velocity, P is the fluid pressure, $e = (\gamma - 1)P$ is the internal energy density ($\gamma = 5/3$ is the adiabatic index), $\mathcal{L}_{cool} = n_e n_i \Lambda$ is the energy loss due to cooling. The AGN terms \mathbf{v}_{jet} , S_ρ , and S_e refer to the jet velocity, density injection, and energy injection due to the jet. We discuss more about the AGN jet implementation in section 3.8.

The gas obeys the ideal gas equation at all times. The pressure is related to the density and temperature as

$$P = \rho k_B T / \mu , \quad (3.7)$$

where μ is the mean molecular mass of the gas. We maintain a floor temperature of 2×10^4 K throughout the grid. If the temperature drops below this floor temperature, the pressure is adjusted (keeping the density the same) in order to reach this floor temperature. This setup gives greater stability to all of the simulations. It is also physically meaningful since the intergalactic medium reaches an approximate state of thermal equilibrium at this temperature.

3.2 The PLUTO Code

PLUTO, developed by A. Mignone et al [22], is a freely-distributed software for numerically solving problems in astrophysical fluid dynamics. The equations are solved on a structured mesh that can be either static or adaptive. The static part of the code is written in the C language, along with a Python module for data analysis and visualization (pyPLUTO). The code supports MPI (Message Passing Interphase) and thus can be parallelized for faster computation. We find that our 1D runs can finish in a reasonable amount of time on a single processor, whereas the 2D runs require a cluster such as SAHA cluster (Physics Department, IISc). The version of the code we use in this work is PLUTO v4.4 (released November 2020).

PLUTO offers a wide range of numerical options and physical modules. The spatial order of reconstruction can be linear, parabolic, etc, and the time stepping can follow the Euler algorithm, RK2, RK3, and others. There are a number of Reimann solvers available, including tvdlf, hll, hllc. Out of these, we find that linear reconstruction with RK2 time stepping and hll solver is the most numerically stable for our purpose. We either turn off the cooling option (for the non-radiative runs) or turn it on (for the cooling flow and AGN feedback runs). For greater numerical stability, we use the CHAR_LIMITING option, which performs reconstruction on the characteristic variables instead of the primitive variables, and we use SHOCK_FLATTENING, which provides additional dissipation in the presence of strong shocks.

The initial and boundary conditions are specified at the runtime initialization, which we describe in section 3.4.

3.3 Dark Matter Halo Evolution

In this work, we do not hydrodynamically evolve the dark matter halo and instead use the formalism described in [3]. These authors use the extended Press-Schechter formalism to show that the average mass history of a wide range of dark matter halos (across masses and cosmologies) follow a universal form. They have presented a FORTRAN code that computes the average and median mass accretion history, the potential well growth history, mass accretion rate, and main progenitor concentration as a function of redshift. It takes the cosmological parameters $\Omega_{m,0}$ (matter fraction), h (reduced Hubble constant), σ_8 (amplitude of the linear power spectrum), $\Omega_{b,0}$ (baryon matter fraction), n (spectral index), and M_0 (mass of the halo at the present redshift) as input parameters and outputs various quantities as a function of redshift in the form of a table. Of importance to us among the outputs is the value of $M(z)/M_0$. In figure 3.1 we plot the growth of the dark matter halo over redshift for a range of masses. The dark matter halo density follows a similar profile to the DK14 profile at all times.

$$\rho_{in}(r) = \rho_{NFW}(r) = \frac{\rho_0}{r/R_s (1 + r/R_s)^2}, \quad (3.8)$$

$$\rho_{out}(r) = \rho_m \left[b_e \left(\frac{r}{5R_{200m}} \right)^{-s_e} + 1 \right], \quad (3.9)$$

$$f_{trans} = \left[1 + \left(\frac{r}{r_t} \right)^\beta \right]^{-\frac{\gamma}{\beta}}, \quad (3.10)$$

$$\rho(r) = \rho_{NFW} f_{trans}(r) + \rho_{out}, \quad (3.11)$$

where R_{200m} (R_{200c}) is the radius where the density of 200 times the mean (critical) density of the universe, $R_S = R_{200c}/c$ where c is the concentration parameter, b_e and s_e are parameters that characterize the density and gravity in the outer regions of the halo, and β , γ , and $r_t = 1.18R_{200m}$ characterize the transition factor. We use the NFW profile to model the inner regions of the halo instead of the Einasto profile because of the numerous studies about the evolution of the concentration parameter. We use the value of $M(z)$ as calculated above in order to calculate the value of R_{200m} and R_{200c} . The values of the parameters b_e and s_e are initially kept constant, and then evolved with time in order to obtain an evolution that gives a universal baryon fraction within halos.

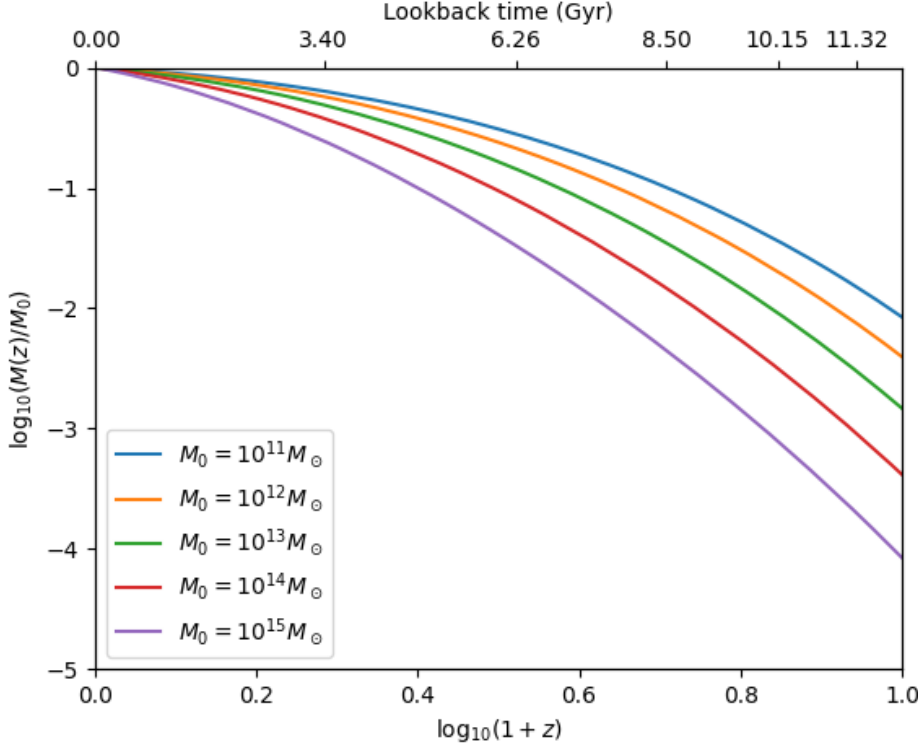


Figure 3.1: Mass accretion histories of dark matter halos with the $z = 0$ mass ranging from 10^{11} to $10^{15} M_{\odot}$. These growth histories are calculated according to [3], using the parameters $\Omega_m = 0.27$, $h = 0.7$, $\sigma_8 = 0.82$, and $n_s = 0.95$. We note that more massive halos grow faster than less massive ones and therefore have larger values of $z_{0.04}$, the redshift when they reach 4% of the mass at $z = 0$ (see equation 3.12).

The concentration parameter c evolves with time, as examined by [47] and [3]. We use the equation

$$c(t) = 4.0 \left[1 + \left(\frac{t}{3.40 t_{0.04}} \right)^{6.5} \right]^{1/8} \quad (3.12)$$

as given by [3], where $t_{0.04}$ is the time at which the main progenitor of a halo gains 4% of its mass at the present redshift. It is straightforward to calculate the value of $t_{0.04}$ from the table of $M(z)$ vs z .

3.4 Grid, Initial, and Boundary Conditions

The baryonic gas is initialized as $\rho_{g,0} = 0.2 \rho_{DM,0}$ at $z = 6$, where $\rho_{DM,0}$ is the dark matter density distribution at $z = 6$. The velocity is initialized as the Hubble velocity, i.e. $v(r) = H(z = 6) r$. The temperature is initialized to a simple profile with high-temperature ($10^7 K$) within the virial radius and low temperature ($10^5 K$) outside it. Except for early transients, our results are mostly independent of the exact choice of initial temperature profile. We start with a series of 1D runs and then move on to 2D axisymmetric runs. We perform our simulations in spherical coordinates with $0 \leq \theta \leq \pi$ and

$$r_{[min,max]} = [0.5, 10^5] \text{ kpc} . \quad (3.13)$$

The θ grid is uniformly spaced. In order to best resolve the AGN jet while also maintaining computational efficiency, the radial grid is uniformly spaced in the innermost 10 kpc and logarithmically spaced outside this. This choice of radial grid gives us the necessary resolution to study both the inner and outer regions of the halo. As all the physical quantities in our problem are independent of ϕ , our 2D simulations are able to shed light on a lot of the underlying mechanisms at work.

We apply outflow boundary conditions at the outer radial boundary (gas is free to leave or enter the computational domain). At the inner radial boundary, we use $dP/dr = -\rho g$ boundary conditions, and we restrict the gas from

entering the computational domain (but is allowed to leave). Reflective boundary conditions are applied in θ (with the sign of v_θ flipped). We noticed that cold gas has a tendency to artificially “stick” at the θ boundaries for our reflective boundary conditions. This cold gas can lead to an unphysically large accretion rate close to the poles, and hence artificially enhanced feedback heating. Therefore, we exclude 0.15 radians of the θ grid at each pole when calculating the mass accretion rate.

3.5 Gravitational Potential

The potentials which correspond to the NFW (inner) and outer profiles corresponding to equations 3.8-3.11 are

$$\Phi(r)_{NFW} = -\frac{4\pi G \rho_0 R_s^3}{r} \ln(1 + r/R_s) , \quad (3.14)$$

$$\Phi(r)_{out} = 4\pi G \rho_m \left(b_e R_{200m}^{s_e} \frac{r^{2-s_e}}{(3-s_e)(2-s_e)} + \frac{r^2}{6} \right) . \quad (3.15)$$

We wish to find an analytic expression for $\Phi(r)$ that will result in a density-potential pair that is consistent with DK14. In other words, we wish to solve

$$\nabla^2 \Phi = 4\pi G(\rho - \rho_m) , \quad (3.16)$$

where ρ_m is the mean density of the universe and $\rho(r)$ is given by equations 3.8-3.11. Since $\rho_{DK14} \rightarrow \rho_{NFW}$ at small radii ($r \ll R_{200}$) and $\rho_{DK14} \rightarrow \rho_{out}$ at large radii ($r \gg R_{200}$), it is natural to take the fitting potential as

$$\Phi(r)_{DM} = w_1 \Phi_{NFW} + w_2 \Phi_{out} , \quad (3.17)$$

where w_1 and w_2 are weight functions.

In order to determine the weight functions, we solve the Poisson equation by the following two methods:

- Method 1: we use the equation

$$\frac{d\Phi(r)}{dr} = \frac{GM_{enc}(r)}{r^2} , \quad (3.18)$$

where $M_{enc}(r) = \int_0^r 4\pi r'^2 \rho(r') dr'$ is the enclosed mass within r . We numerically integrate equation 3.18 to get $\Phi(r)$.

- Method 2: we directly calculate $\Phi(r)$ by numerically integrating the equation

$$\Phi(r) = -4\pi G \left[\frac{1}{r} \int_0^r \rho(r') r'^2 dr' + \int_r^\infty \rho(r') r' dr' \right] . \quad (3.19)$$

Both of these methods give similar results, allowing use to construct an analytic potential which fits the numerical result:

$$w_1 = 1 - \left(\frac{1 + erf(x)}{c_e} \right) \quad w_2 = (1 - w_1^4)^{1/4} , \quad (3.20)$$

where $erf(x)$ is the error function, $x = \log(r/r_t)$, and c_e ranges from 5 to 10, dependent on ν , R_{200m} , s_e , and other input parameters. The density-potential pair for our fitting potential as well as those constructed by the above two methods are shown in figure 3.2. We note that our constructed potential corresponds to the density $\rho(r)_{DK14} - \rho_m$ and not $\rho_{DK14}(r)$ itself, as the mean density of the universe will not have any contribution to the gravitational potential/acceleration of an individual halo. This is why the density plot in figure 3.2 is monotonically decreasing with radius, whereas in equation 3.9, we see that the density asymptotes to ρ_m .

The above potential accounts for the gravitational potential due to the dark matter halo, which causes an inward gravitational acceleration toward the center of the halo. However, the gas at the outer parts of the computational domain, far from the virial radius, should be flowing radially outward. The velocity follows Hubble's law $v = H(z)r$. In order to ensure this behavior, we add a cosmological potential Φ_{cos} such that the gas follows

$$M_0 = 10^{14} M_\odot$$

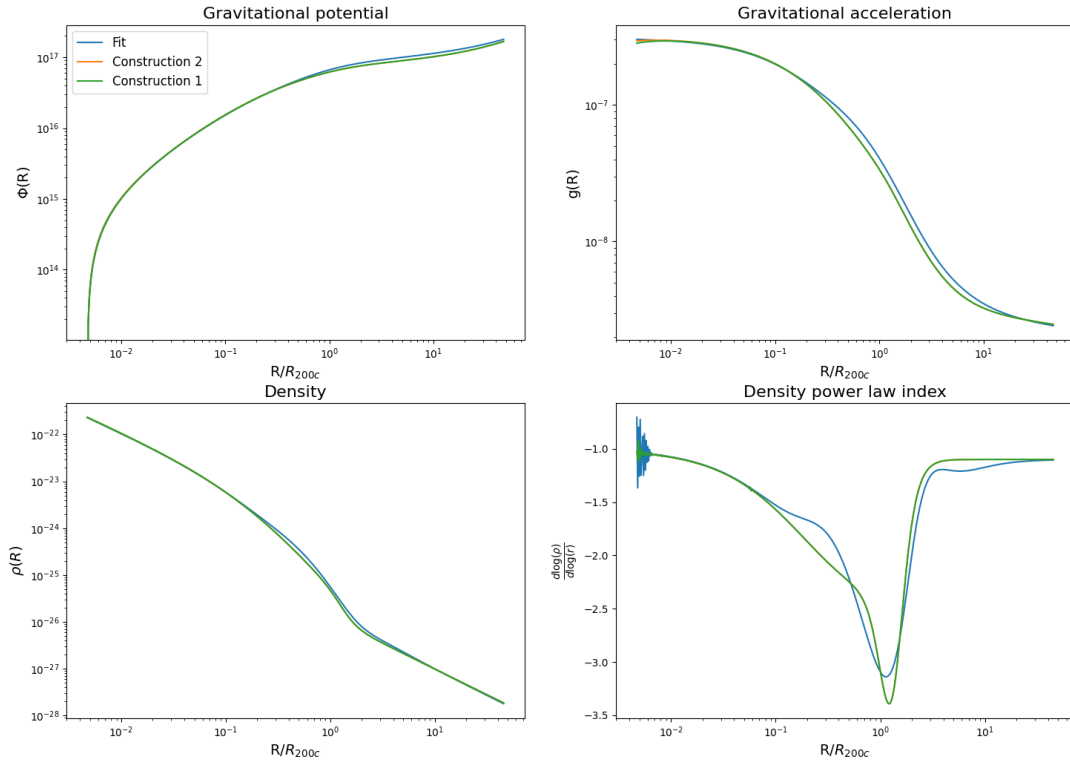


Figure 3.2: Gravitational potential, acceleration, density, and the local density power law index ($d \ln \rho / d \ln r$) as a function of radius given by equations 3.18 and 3.19. The halo mass is $M_0 = 10^{14} M_\odot$ and the concentration parameter c is set to 4.

Hubble's law at all times far from the halo.

The velocity evolves as

$$\frac{\partial v}{\partial t} = -v \frac{\partial v}{\partial r} + g, \quad (3.21)$$

where $g = -\frac{d\Phi}{dr}$ is the gravitational acceleration due to the cosmological potential. For Hubble expansion, $-v \frac{\partial v}{\partial r} = -H^2 r$ and $\frac{\partial v}{\partial t} = \dot{H} r$. Therefore, for a consistent evolution, we have

$$g = (\dot{H} + H^2)r \quad \Phi_{cos} = -(\dot{H} + H^2) \frac{r^2}{2}. \quad (3.22)$$

For a flat Universe, the Hubble parameter evolves as $H(z)^2 = H_0^2 E(z)^2$ where $E(z)^2 = \Omega_m(1+z)^3 + \Omega_\Lambda$.

$$\dot{H} = -H^2 \frac{d \ln E}{d \ln(1+z)} = -\frac{3H^2 \Omega_m(z)}{2}, \quad (3.23)$$

where $\Omega_m(z) = \Omega_{m,0} \frac{(1+z)^3}{E(z)^2}$ is the redshift-dependent matter fraction. Substituting in equation 3.23, we have

$$\Phi(r)_{cos} = -H^2 \left(1 - \frac{3\Omega_m(z)}{2}\right) \frac{r^2}{2}. \quad (3.24)$$

The total potential is $\Phi(r) = \Phi(r)_{DM} + \Phi(r)_{cos}$, which accounts for the gravitational potential of the halo as well as leads to an evolution consistent with Hubble's law at all times.

3.6 Radiative Cooling

We implement radiative cooling using the cooling function given by equation 4 of [44]. This function was calculated by running photoionization models and calculating the element-by-element cooling rates under exposure to the cosmic microwave background radiation.

$$\Lambda = \Lambda_{H,He} + \sum_{i>He} \Lambda_{i,\odot} \left(\frac{n_e}{n_{e,\odot}} \right) \left(\frac{n_i}{n_{i,\odot}} \right) \quad (3.25)$$

where the first term corresponds to the cooling due to Hydrogen and Helium, and the second term corresponds to all the other elements (metals). We use the cooling function table given in [44], which lists the contribution of $\Lambda_{H,He}$ and Λ_Z for the solar metallicity as a function of temperature. The calculation of the cooling function becomes straightforward:

$$\Lambda(T) = \Lambda_{H,He} + \frac{Z}{Z_\odot} \Lambda_Z \quad (3.26)$$

As we can see in figure 3.3, the cooling function strongly depends on the metallicity of the gas. The metallicity of the diffuse, condensed, and warm-hot intergalactic medium is well studied by several authors ([45], [24], [26]). We use a simple analytic fit for the metallicity as a function of redshift:

$$\log(Z(z)/Z_\odot) = \begin{cases} -0.52 - 0.25z & r < R_{200} \\ -2 - 0.5z & r > R_{200} \end{cases} \quad (3.27)$$

This fit evolves the metallicity within the halo from $0.01Z_\odot$ at $z = 6$ to $0.3Z_\odot$ at $z = 0$. The value of $0.3Z_\odot$ at the present redshift is chosen to match observations of the interstellar medium (ISM). The metallicity is kept low outside the halo, evolving from $10^{-5}Z_\odot$ at $z = 6$ to 10^{-2} at $z = 0$.

3.7 Evolution of the Central Supermassive Black Hole

We place a seed black hole at the center of the halo at $z = 6$ and evolve the black hole mass in our simulations. The black hole grows by the accretion of cold gas onto its event horizon. We relate the value of \dot{M}_{acc} to the infalling mass at a boundary of our computational domain \dot{M}_{in} by the parameter ϵ_m , the efficiency of mass transport from the inner boundary to the BH event horizon. This value is the fraction of cold gas at the inner

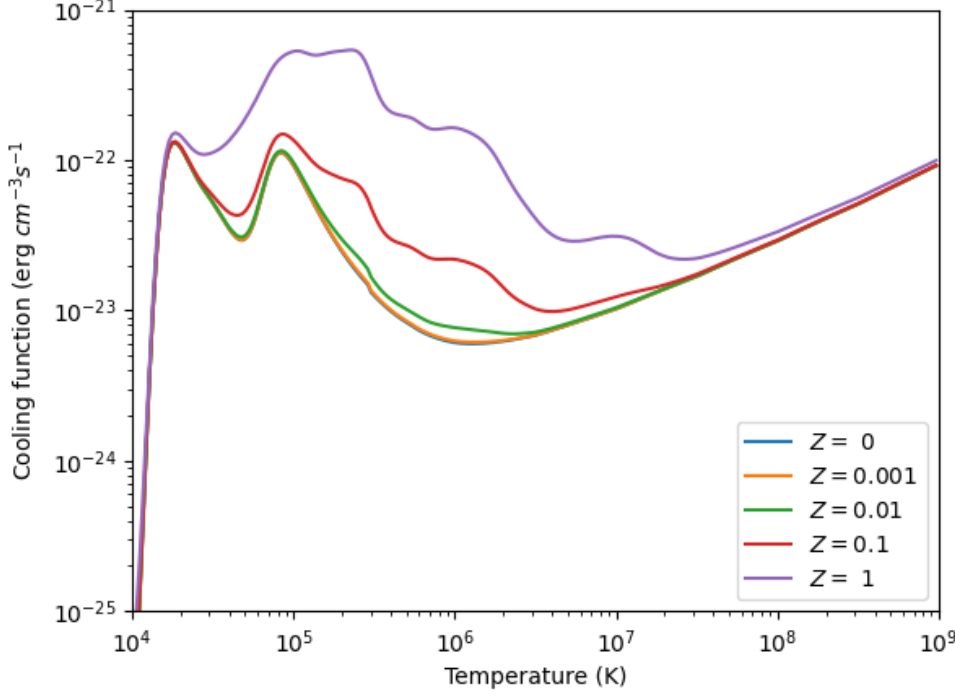


Figure 3.3: The cooling function (see Eq. 3.26) that we implement for various metallicities, as described by [44]. The value of Λ is strongly dependent on the metallicity, which suggests that the metallicity evolution of the ICM and the IGM plays an important role for gas cooling within halos.

boundary that reaches the event horizon of the black hole, and is typically taken to be $10^{-4} - 10^{-2}$.

$$\dot{M}_{acc} = \epsilon_m \dot{M}_{in} = \begin{cases} \epsilon_m 4\pi r_{in}^2 \rho_{in} v_{in}|_{\text{cold}} & \text{in 1D} , \\ \epsilon_m 2\pi r_{in}^2 \int \rho_{in} v_{int} \sin \theta d\theta|_{\text{cold}} & \text{in 2D} . \end{cases} \quad (3.28)$$

In the 2D runs, we notice that the gas has a tendency to "stick" to the θ -boundaries and cool to the floor temperature. The reason for this phenomenon is the reflective boundary conditions in the θ direction that we have implemented and the axisymmetry assumed. This can artificially increase the value of \dot{M}_{in} to unphysical values and lead to enhanced AGN feedback. In order to prevent this, we exclude 0.15 radians of θ centered at each pole in the calculation of \dot{M}_{in} . This corresponds to a very small solid angle, so we still consider the majority of the gas flowing through the inner boundary.

At each computational step, the mass of the black hole is grown by

$$\Delta M_{BH} = \dot{M}_{acc} \times \Delta t . \quad (3.29)$$

As mentioned earlier, the velocity at the innermost boundary of the computational domain is subject to the boundary conditions and the resulting \dot{M}_{in} is not very stable. Therefore, we evaluate \dot{M}_{in} at around 1 kpc, which is just slightly outside of the innermost boundary of 0.5 kpc, but not too influenced by the boundary conditions.

The total efficiency of the AGN jet is given by

$$\epsilon = \epsilon_m \times \epsilon_{BH} , \quad (3.30)$$

where ϵ_{BH} is the black hole feedback efficiency, the fraction of the accretion rate that is converted to radiation or mechanical energy. We set the value of ϵ_{BH} to be 0.1. We consider a simplified model where both of these parameters are taken to be constant in time.

The accretion rate is limited by the Eddington rate of the black hole at any point of time:

$$\dot{M}_{Edd} = \frac{4\pi GM_{BH}m_p}{\epsilon_{BH}\sigma_{Tc}}, \quad (3.31)$$

which is a function of M_{BH} and ϵ_{BH} . The accretion rate is then taken as the maximum of that calculated in equation 3.28 and \dot{M}_{Edd} . As the black hole grows in mass, the Eddington rate increases and a greater accretion rate is allowed. In addition, a lower accretion efficiency implies that more mass can accrete onto the black hole before reaching the Eddington limit, leading to faster growth of the black hole.

3.8 AGN Jet Feedback

The AGN jet is implemented in the computational domain using a source term at the innermost region. The implementation of the jet is similar to that of [29]; here we summarize the important points.

The density source term is given by

$$\dot{S}_\rho(r, \theta) = \mathcal{N}\dot{M}_{jet}\psi(r, \theta) \quad (3.32)$$

where ψ is the geometrical factor that smoothly falls to zero outside the biconical region of radius r_{jet} and half-opening angle θ_{jet}

$$\psi(r, \theta) = \left[2 + \tanh\left(\frac{\theta_{jet} - \theta}{\sigma_\theta}\right) + \tanh\left(\frac{\theta_{jet} + \theta - \pi}{\sigma_\theta}\right) \right] \times \left[1 + \tanh\left(\frac{r_{jet} - r}{\sigma_r}\right) \right] \times \frac{1}{4} \quad (3.33)$$

and \mathcal{N} is the normalization factor

$$\mathcal{N} = \frac{3}{2\pi r_{jet}^3 (1 - \cos\theta_{jet})} \quad (3.34)$$

The mass infall rate \dot{M}_{in} is calculated as the cold gas mass flux within an inner boundary r_b . As the velocity at innermost boundary is subject to oscillations due to the boundary conditions, we evaluate the infalling mass at r_{in} which is slightly outside the innermost boundary at 1 kpc. We note that \dot{M}_{in} is limited by the Eddington luminosity of the central SMBH. The mass loading rate is then calculated as

$$\dot{E}_{jet} = \epsilon_{BH}\dot{M}_{acc}c^2 = \epsilon\dot{M}_{in}c^2 \quad (3.35)$$

where $\epsilon = \epsilon_m \times \epsilon_{BH}$ is the total AGN feedback efficiency. We select the parameters $r_{jet} = 2$ kpc, $\theta_{jet} = \pi/6$, $\sigma_r = 0.05$ kpc, $\sigma_\theta = 0.05$, and $v_{jet} = 3 \times 10^4$ km/s for all our simulations. The results are largely insensitive to the exact values of these parameters. The efficiency of the feedback ϵ , however, is an important parameter that strongly influences the evolution.

The total feedback from the AGN is released into the ICM as kinetic (mechanical) and thermal energy. We introduce a parameter f_{kin} as the fraction of energy that is released as kinetic energy, and $1 - f_{kin}$ is the fraction released as thermal energy. Therefore, we have

$$\dot{E}_{kin} = \dot{M}_{jet}v_{jet}^2 = f_{kin}\dot{E}_{jet} \quad (3.36)$$

where $\dot{M}_{jet} = 0.5\eta_{MLF}\dot{M}_{acc}$ and η_{MLF} is the single jet mass loading factor, which we set to 1. The thermal energy injection is then

$$\dot{E}_{th} = \dot{E}_{jet} - \dot{E}_{kin} = (1 - f_{kin})\dot{E}_{jet} \quad (3.37)$$

The source density and energy terms are then added to the non-conservative forms of the Euler equations as

$$\rho(r, \theta)_+ = \psi(r, \theta)\mathcal{N}\dot{M}_{jet}\Delta t \quad (3.38)$$

$$P(r, \theta)_+ = \psi(r, \theta)\mathcal{N}\dot{E}_{th}(\gamma - 1)\Delta t \quad (3.39)$$

The kinetic fraction f_{kin} is set to 0.5 in all our runs.

Chapter 4

Results

4.1 Non-Radiative Runs

We start with 1D simulations in the absence of radiative cooling and AGN feedback. For all halos, we keep the outer density parameters s_e and b_e constant as $s_e = 1.5$ and $b_e = 2.5$.

The density, pressure, velocity, and temperature profiles for a halo mass $M_0 = 10^{14} M_\odot$ are shown in figure 4.1. We can see that in the absence of heating and cooling, a core is formed that extends up to $\sim 10^{-2} R_{200c}$, similar

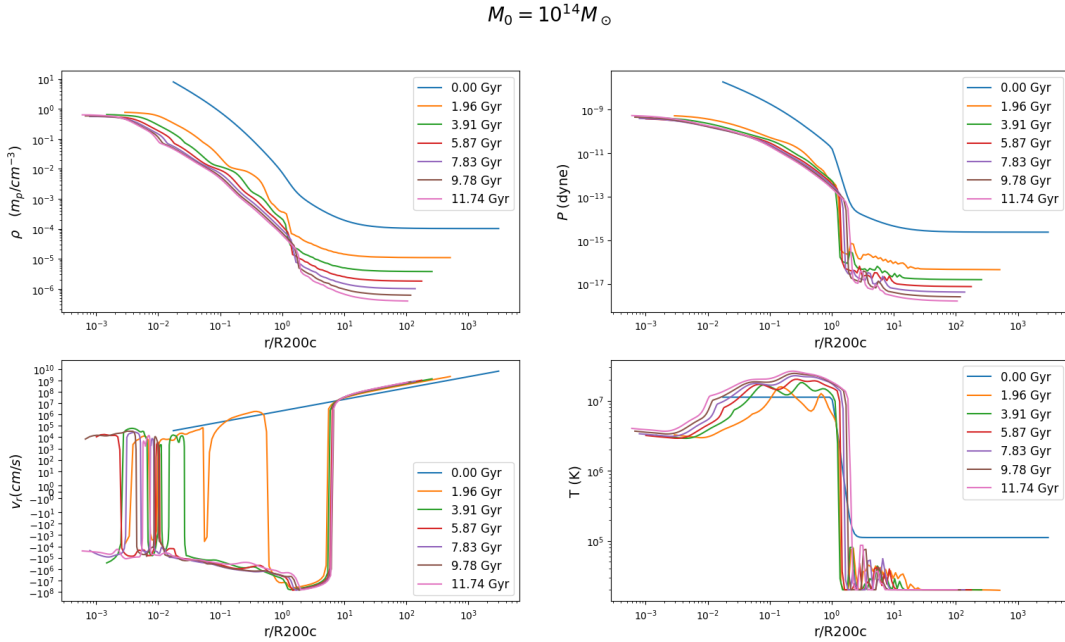


Figure 4.1: Density, pressure, velocity, and temperature profiles for the non-radiative runs with $M_0 = 10^{14} M_\odot$. The inner halo ($< 10^{-2} R_{200c}$) gas shows a core, with a nearly constant temperature and density. The gas at the outer radii $> 10 R_{200c}$ are driven by Hubble expansion, with velocity linearly increasing with radius as $v = H(z)r$. This adiabatic expansion leads to a low temperature in the outer regions.

to the results of [4]. This region has a lower temperature (few $\times 10^6 K$ for $M_0 = 10^{14} M_\odot$) compared to the near the virial radius. It is also characterized by the flattening of the density profile.

In the absence of cooling, the velocities within the virial radius are small and mostly random due to the adiabatic nature of the gas. The gas behaves adiabatically within the shock radius, where the gravity due to the dark matter is much stronger than the gravity due to the cosmological potential (equation 3.24).

4.1.1 Hubble Expansion

At around $10R_{200}$, the velocity is completely radially outward and follows $v(r) = H(z)r$. This is because of the introduction of cosmological potential (equation 3.24), which ensures consistency with Hubble's law. As $H(z) \propto E(z)$, we expect that the velocity at the outermost point of the active zone should evolve as $v_{out} \propto r_{out}E(z)$. This is verified in figure 4.2.

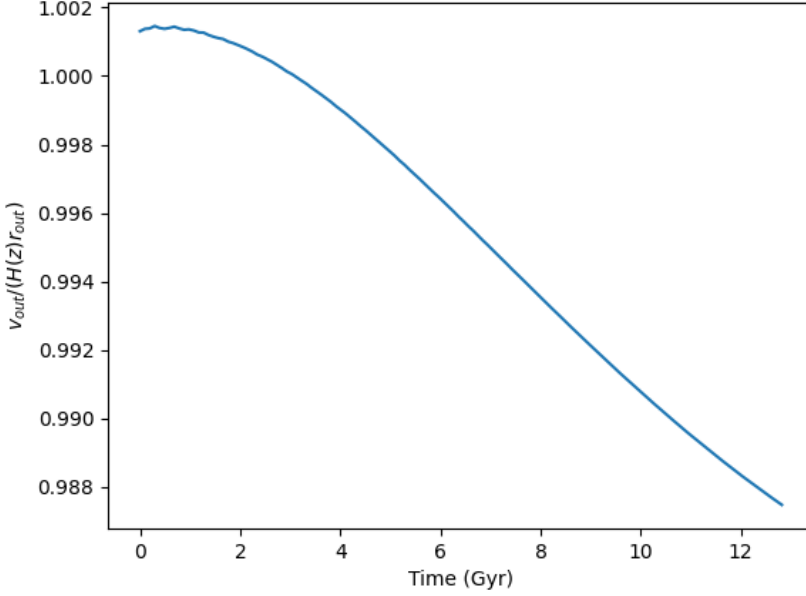


Figure 4.2: Plot of $v_{out}/(H(z)r_{out})$ (outer radial velocity scaling with time-dependent Hubble expansion) as a function of time for $M_0 = 10^{14}M_\odot$. Note that the outer velocity closely follows Hubble expansion due to the cosmological potential (equation 3.24).

4.1.2 Formation of the Virial Shock

The formation of the virial shock occurs through multiple stages (see [1] for a review). Because of our choice of the initial temperature profile, shocks are formed at early times but they are not stationary. We can see that for $M_0 = 10^{14}M_\odot$, before 1.17 Gyr ($z \approx 3.1$) the virial shock is not fully formed yet and consists of a weak shock near the virial radius and a somewhat smooth transition to the outer regions, whereas after $z \approx 3.1$ the shock is fully localized at near the virial radius. This shock formation redshift z_s depends on the halo mass, and is smaller for more massive halos.

4.1.3 Baryon Fraction Evolution

We define the baryon fraction within a radius r as the gas fraction within that radius, namely

$$f_b = \frac{\int_0^r \rho_g(r')r'^2 dr'}{\int_0^r \rho_{DM}(r')r'^2 dr' + \int_0^r \rho_g(r')r'^2 dr'} , \quad (4.1)$$

with ρ_g and ρ_{DM} being the gas and dark matter density respectively. We initialize the gas density such that the fraction is $f_b(z=6) = 1/6$ (the universal baryon fraction) at all radii. In figure 4.4, we plot the baryon fraction as a function of r at later times for our non-radiative/non-feedback runs. We see that the baryon fraction is smaller than the universal baryon fraction at all radii $< 100R_{200c}$. This suggests that a value of $s_e = 1.5$ does not provide enough inward gravitational acceleration in the outer regions of the halo. As a result, an insufficient amount of gas falls inside the virial radius to maintain a universal baryon fraction. We modify the parameters b_e and s_e (see equation 3.9) to maintain a universal baryon fraction in section 4.2.

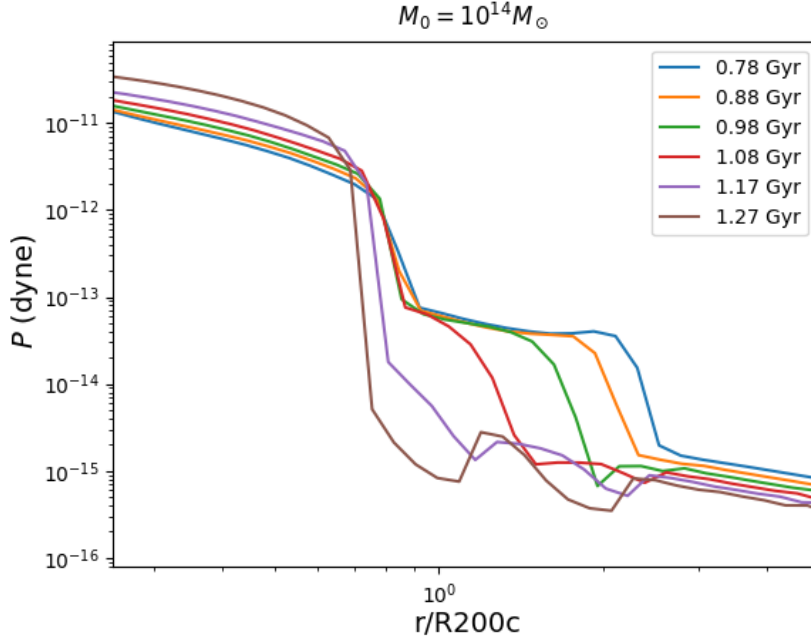


Figure 4.3: Formation of the virial shock for $M_0 = 10^{14}M_\odot$ as seen in this pressure versus radius plot at early times. We can see that the shock is not stationary at early times, and slowly transitions to a localized shock near R_{200c} .

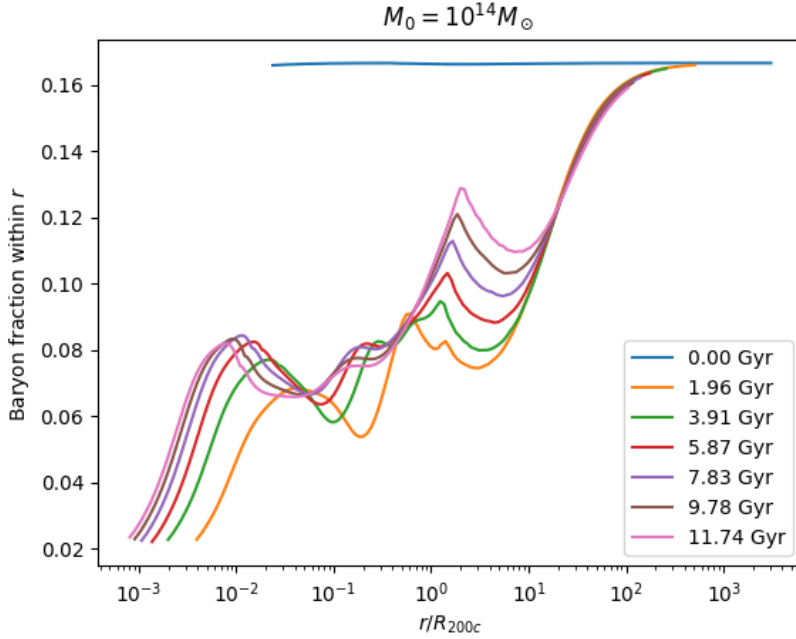


Figure 4.4: Baryon fraction as a function of radius for $M_0 = 10^{14}M_\odot$ for non-evolving DK14 parameters $s_e = 1.5$ and $b_e = 1.5$. This choice of parameters result in a baryon fraction that is lesser than the universal value within the virial radius at all times.

4.1.4 Self-Similar Evolution

In figure 4.5, we plot the gas density as a function of the scaled radius r/R_{200c} for various halo masses at a redshift of $z = 1$ and $z = 0$ respectively. The inner regions show variations in the profile due to the differences in the core temperature. However, we can see that the regions $> 0.03R_{200c}$ behave reasonably self-similar with respect to the virial radius.

This self-similar behavior of the gas across a large range of halo masses can be understood by considering the

gravitational potential $\Phi(r)$ given by equation 3.16. The characteristic density and length scales are given by

$$\rho_0 = \frac{200c^3\rho_c}{3\left(\log(1+c) - \frac{c}{1+c}\right)}, \quad (4.2)$$

and

$$R_{200c} = \left(\frac{3M_{200}}{800\pi\rho_c}\right)^{1/3}, \quad (4.3)$$

where ρ_c is the critical density of collapse at any redshift.

The gravitational potential in the small r and large r limit are given by $\Phi(r) \approx \Phi_{NFW}(r)$ and $\Phi(r) \approx \Phi_{out}(r)$ respectively. The self-similar behavior of these two quantities is examined below:

$$\Phi_{NFW}(r) = -\frac{4\pi G\rho_0 R_s^3}{r} \ln(1+r/R_s). \quad (4.4)$$

In the small r limit, we have

$$\vec{g}_{NFW}(r) \propto \frac{\frac{r}{R_s} - \ln(1+r/R_s)}{(r/R_s)^3} \frac{\vec{r}}{R_s}, \quad (4.5)$$

which is a function of only $r/R_s = r/R_{200c} \times c$. Likewise, the potential and acceleration in the outer region is

$$\Phi(r)_{out} = 4\pi G\rho_m \left(b_e R_{200m}^{s_e} \frac{r^{2-s_e}}{(3-s_e)(2-s_e)} + \frac{r^2}{6} \right), \quad (4.6)$$

$$\vec{g}_{out}(r) \propto \left(\frac{r}{R_{200m}} \right)^{-s_e} \frac{\vec{r}}{R_{200m}}, \quad (4.7)$$

which is self-similar in $r/R_{200m} \approx r/R_{200c}$. We therefore expect the gas to behave self-similarly in both the inner and outer regions of the halo at all times (after the initial transients). The deviations from self-similarity are the greatest near the virial shock, where the inner and outer profiles are patched together.

We note that the concentration parameter c is itself a function of the halo mass and the formation redshift (equation 3.12). The halo mass dependence of c can be ignored compared to that of r .

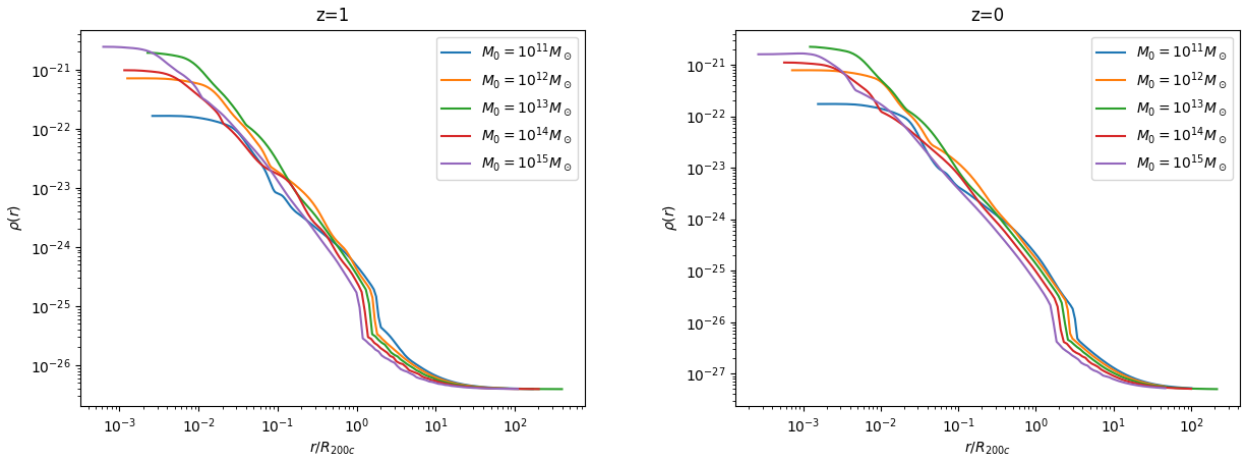


Figure 4.5: Density (ρ) versus scaled radius (r/R_{200c}) for different halo masses at $z=1$ (left panel) and $z=0$ (right panel). In the absence of radiative cooling and feedback, the density profiles are reasonably self-similar with respect to the halo mass at all times after the initial transients.

4.2 Maintaining a Constant Baryon Fraction

We saw in section 4.1.3 that a constant value of the parameters $b_e = 2.5$ and $s_e = 1.5$ of the DK14 profile underestimates the baryon fraction of the halo. The baryon fraction within a radius of $\approx 0.1R_{200c}$ depends

Table 4.1: Results of the non-radiative runs. The core temperature and the virial temperature (temperature at R_{200c}) both increase with halo mass.

Halo Mass at $z = 0$	$z_{0.04}$	T_{core} (K)	ρ_{core} (m_p/cm^3)	T_{vir} (K)	ρ_{vir} (m_p/cm^3)	R_{200c} (kpc)
$10^{11}M_{\odot}$	5.8332	3.28×10^5	1.09×10^{-2}	1.21×10^5	1.87×10^{-5}	95.91
$10^{12}M_{\odot}$	4.8747	7.51×10^5	4.43×10^{-1}	4.89×10^5	1.59×10^{-5}	206.62
$10^{13}M_{\odot}$	3.9257	1.45×10^6	1.33	2.36×10^6	1.54×10^{-5}	445.17
$10^{14}M_{\odot}$	3.0139	4.31×10^6	6.26×10^{-1}	1.28×10^7	1.57×10^{-5}	959.09
$10^{15}M_{\odot}$	2.179	1.10×10^7	9.52×10^{-1}	7.08×10^7	1.30×10^{-5}	2066.29

strongly on the physics of the gas (radiative cooling, AGN feedback, supernova feedback, etc) [19] [10]. The baryon fraction of clusters has been studied extensively from observations [33] [13], large-scale hydrodynamical simulations [32] [20] [28], and cosmological N-body simulations [8]. It is clear from these studies that the baryon fraction near the virial radius is within $\sim 20\%$ of the universal baryon fraction, and it has a slight dependence on halo mass. The baryon fraction around and outside the virial radius depends mostly on only the gravitational potential/acceleration of the dark matter. Therefore, we modify the parameters of the dark matter halo in order to achieve the universal baryon fraction beyond R_{200c} .

We note in figure 4.4 that the baryon fraction up to $\sim 100R_{200c}$ is significantly lower than the universal value of $1/6$, and reaches this value at around $\sim 100R_{200c}$. Therefore, our goal is to increase the inward gravitational acceleration in the outer regions of the computational domain, in order to cause more gas to flow towards the halo and increase the baryon fraction. We note that for a density $\rho(r) \propto r^{-\gamma}$, the potential and acceleration corresponding to this will be

$$\Phi(r) \propto r^{\gamma+2}, \quad g(r) \propto r^{\gamma+1}. \quad (4.8)$$

Therefore, a lower value of s_e in the DK14 density profile corresponds to increased gravity in the outer regions, and increased baryon fraction throughout the halo.

The parameter b_e also plays an important role in the gas evolution. Our results indicate that a higher value of b_e leads to a larger baryon fraction around R_{200c} , whereas the regions $> 10R_{200c}$ are relatively unaffected by the value of b_e .

We test various value of b_e and s_e for various halo masses, and found that we can closely match the universal baryon fraction at all times by introducing a redshift dependence on the parameters. In table 4.2, we list the expressions for s_e and b_e that we found will achieve universal baryon fraction near and outside R_{200c} . In figure 4.6, we plot the baryon fraction of an adiabatic run with $M_0 = 10^{14}M_{\odot}$, using the expressions listed in table 4.2. We see that the baryon fraction lies within $\sim 15\%$ of the universal value at all times after the initial 2 Gyr.

Table 4.2: DK14 parameters for different halo masses for maintaining universal baryon fraction.

Halo Mass at $z = 0$	$s_e(z)$	$b_e(z)$
$10^{12}M_{\odot}$	$1.4 - 0.033z$	$1.2 + 0.083z$
$10^{14}M_{\odot}$	$1.5 - 0.033z$	$1.2 + 0.583z$
$10^{15}M_{\odot}$	$1.1 - 0.016z$	$2.0 + 0.5z$

4.3 Runs with Radiative Cooling

We now implement radiative cooling in our runs. The metallicity-dependent cooling function is described in section 3.6, and we evolve the metallicity of the computational domain (halo+intergalactic medium) according to equation 3.27.

We maintain the same initial conditions as described in section 4.1. We note that as compared to the adiabatic runs, the runs with cooling are more sensitive to the initial conditions. If the initial temperature within the halo is set too low, cooling dominates immediately and no stable virial shock is formed at any time.

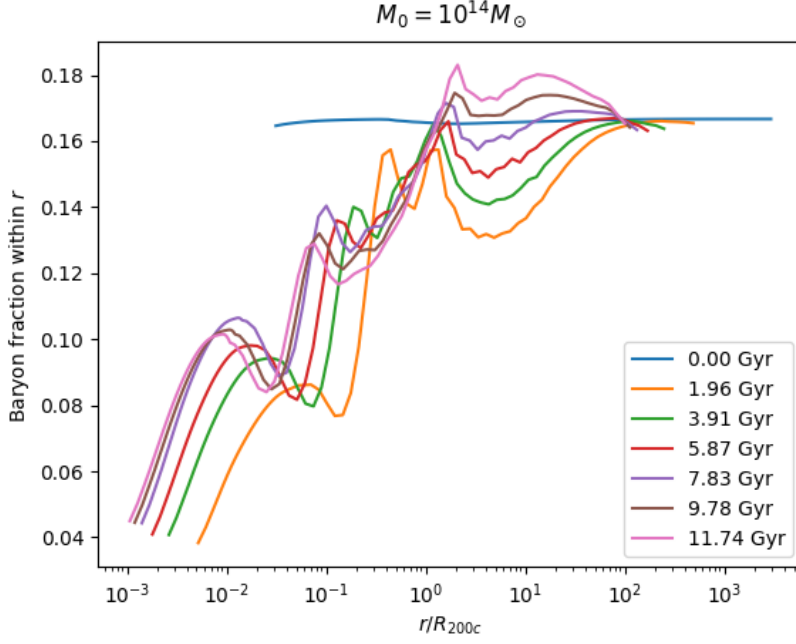


Figure 4.6: Baryon fraction evolution for a non-radiative run with $M_0 = 10^{14} M_\odot$, using the redshift-dependent parameters for s_e and b_e listed in table 4.2. Using these values, the baryon fraction at the virial radius is close to the universal value at all times. As the parameters s_e and b_e characterize the outer profile, the inner radii ($r < 10^{-1} R_{200c}$) are unaffected by this change in parameters.

Our choice of initial temperature profile ensures that a stable virial shock is formed at an early time for high-mass halos ($M_0 \geq 10^{14} M_\odot$), as shown in multiple studies [1] [18].

4.3.1 Lower Mass Halos

We start with low mass halos ($M_0 < 10^{12} M_\odot$). In figure 4.7, we plot the density, pressure, velocity, and temperature profiles for a cooling flow run with $M_0 = 10^{12} M_\odot$. With our implementation of radiative cooling as

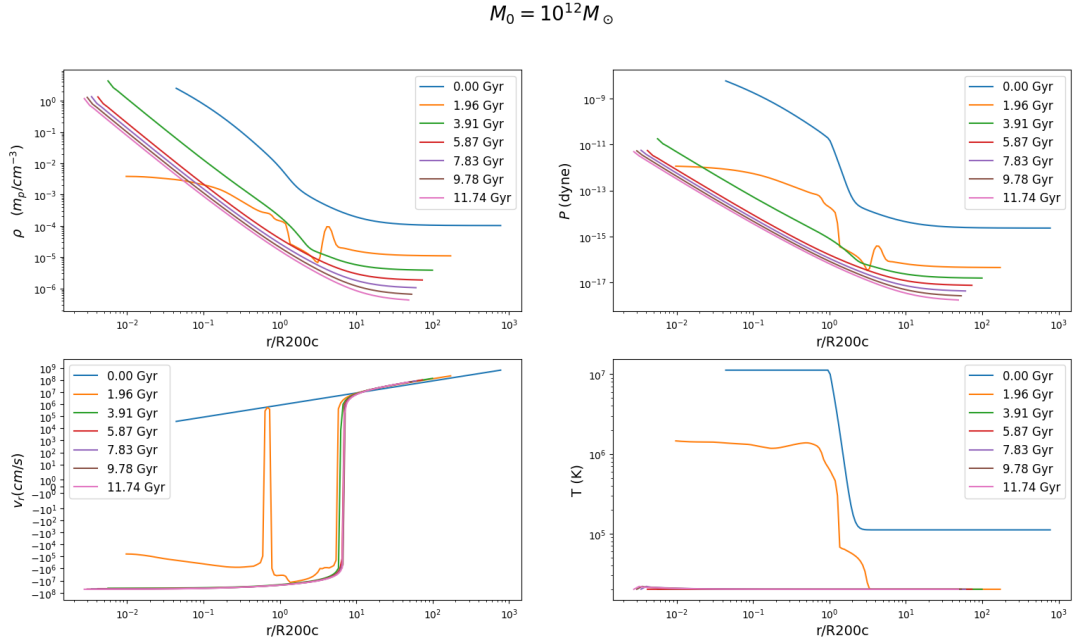


Figure 4.7: Cooling flow profiles for $M_0 = 10^{12} M_\odot$. The gas quickly cools to the floor temperature and no virial shock is formed.

given by equations 3.26, we can see that lower mass halos are unable to form a stable pressure-supported virial shock. The profiles in the initial 2 Gyr are transient states where neither cooling dominates nor the gas behaves adiabatically. These states correspond to the high-redshift state of the IGM with a low metallicity. After the initial ~ 2.5 Gyr, cooling dominates at all radii $< 10R_{200c}$, and the temperature drops to the floor temperature at all points. [1] find that the critical mass below which the cold accretion dominates at all times is $\approx 3 \times 10^{11} M_\odot$, while Choudhury et al (2019) [4] found that the value is slightly lower at $\approx 10^{11} M_\odot$.

The velocity is radially inwards at all points $< 10R_{200c}$ (the turn-around radius). There is no sudden drop in velocity near R_{200c} corresponding to a virial shock. This cooling flow results in a high mass accretion rate at the inner boundary. At outer radii $> 10R_{200c}$, the cosmological potential dominates and causes the velocity to be radially outward, consistent with Hubble expansion.

We can understand the behavior of the cooling flow runs by analysing the ratio of the cooling time to the free-fall time, i.e. t_{cool}/t_{ff} . The timescales are given by

$$t_{cool} = \frac{3}{2} \frac{nk_B T}{n_i n_e \Lambda(T)}, \quad (4.9)$$

$$t_{ff} = \left(\frac{2r}{g} \right)^{1/2}. \quad (4.10)$$

We can see that at points of time after the initial transient states, the value of t_{cool}/t_{ff} is less than 1 at all

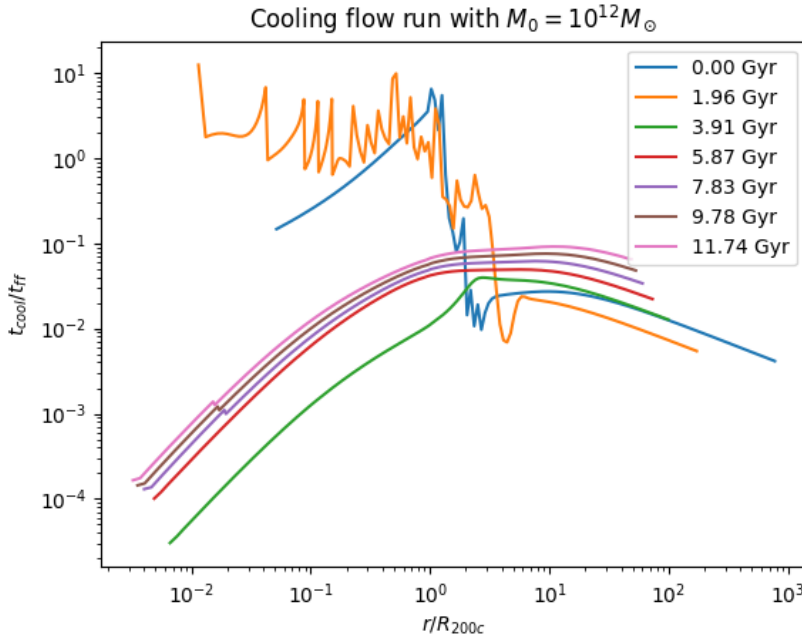


Figure 4.8: t_{cool}/t_{ff} vs r for $M_0 = 10^{12} M_\odot$ with radiative cooling. The values are small at all times after the initial transients, which correspond to a strong cooling flow.

radii. Stern et al (2021) [40] analyze the FIRE-2 cosmological simulations [15] and find that $t_{cool} \approx t_{ff}$ somewhere between $0.1R_{vir} - 0.5R_{vir}$ for intermediate mass halos ($10^{11} - 10^{12} M_\odot$). However, they only consider cool gas $T < 10^{4.5} K$ in their calculations, and there are several differences in our setup compared to the full cosmological simulations. They mention that idealized hydrodynamical simulations give $t_{cool} \ll t_{ff}$ when the temperature is lesser than the virial temperature of the halo.

4.3.2 Higher Mass Halos

For higher mass halos ($M_0 > 10^{13} M_\odot$), the radiative cooling dominates in the inner regions of the halo ($r < 0.1R_{200}$), resulting in a temperature significantly lower than the that of the corresponding adiabatic run. The density near the center shows a cusp-like behavior instead of a core, which occurs in adiabatic runs. In figure 4.9

we show the profiles corresponding to the cooling flow runs of a $M_0 = 10^{14} M_\odot$ halo.

The plot of t_{cool}/t_{ff} for this run is shown in figure 4.10. We can see that $t_{cool}/t_{ff} < 1$ for $r < 0.01 R_{200c}$, which

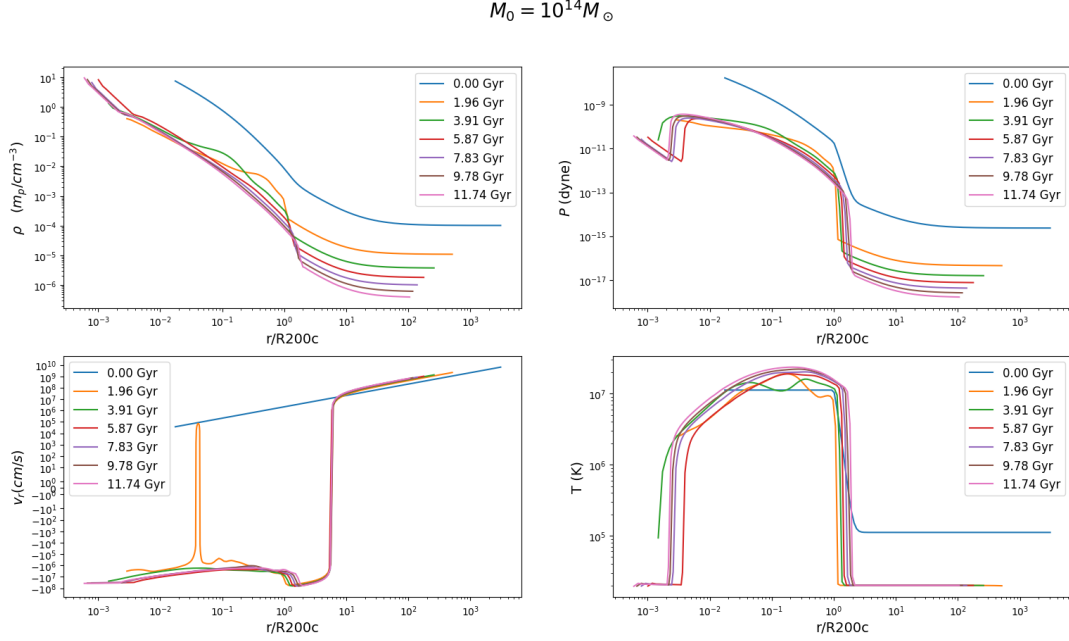


Figure 4.9: Cooling flow profiles for $M_0 = 10^{14} M_\odot$. For this halo mass, the radiative cooling strongly affects the inner regions, as the density profile is cuspy instead of core-like and the temperature decreases compared to the non-radiative runs (figure 4.1). However, the regions $> 10^{-1} R_{200c}$ behave very similar to the non-radiative runs, and a stable virial shock is still formed.

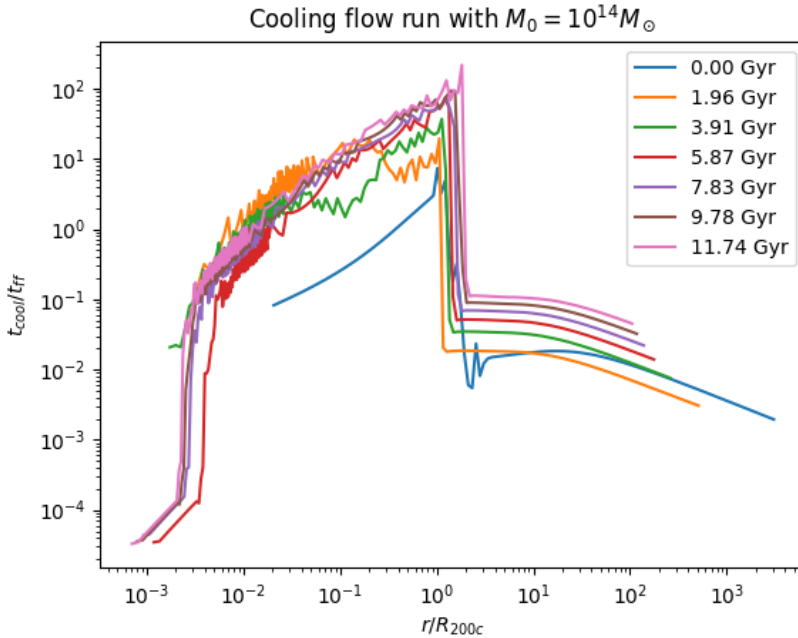


Figure 4.10: The ratio of the cooling time to the free-fall time (t_{cool}/t_{ff}) versus radius for $M_0 = 10^{14} M_\odot$ with radiative cooling. This quantitatively illustrates that only the innermost regions are subject to a strong cooling flow, while the outer regions have a high value of t_{cool}/t_{ff} and are mostly unaffected by cooling.

corresponds to a strong cooling flow. However, its value for $r > 0.1 R_{200c}$ is greater than 10, implying that the regions near the virial shock are relatively unaffected by cooling. The formation of the shock occurs through several transients as before, and occurs at a slightly early time compared to the adiabatic run, as we can see in

figure 4.11.

The cuspy behavior of the gas at small radii causes the baryon fraction at the inner region to substantially

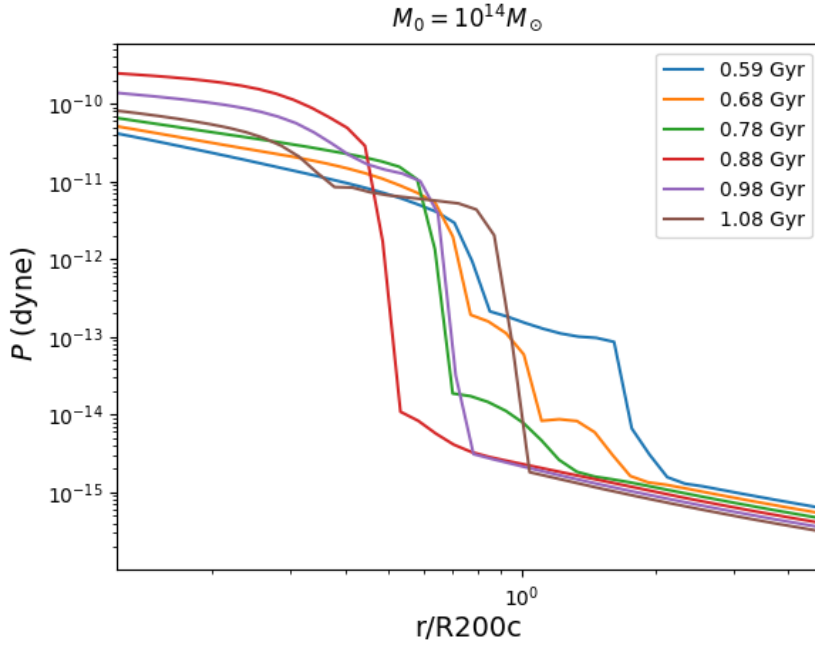


Figure 4.11: Formation of virial shock for a cooling flow run with $M_0 = 10^{14} M_\odot$.

increase beyond the universal baryon fraction. However, if we use the same redshift-dependent parameters for the outer DK14 profile as in the adiabatic runs, the baryon fraction in the regions relatively unaffected by cooling ($> 0.1 R_{200}$) behaves similarly as the adiabatic case. In the inner parts of the halo, the baryon fraction is significantly greater than the corresponding adiabatic run.

The strong cooling in the inner regions of the halo leads to a very large accretion rate at the inner boundary.

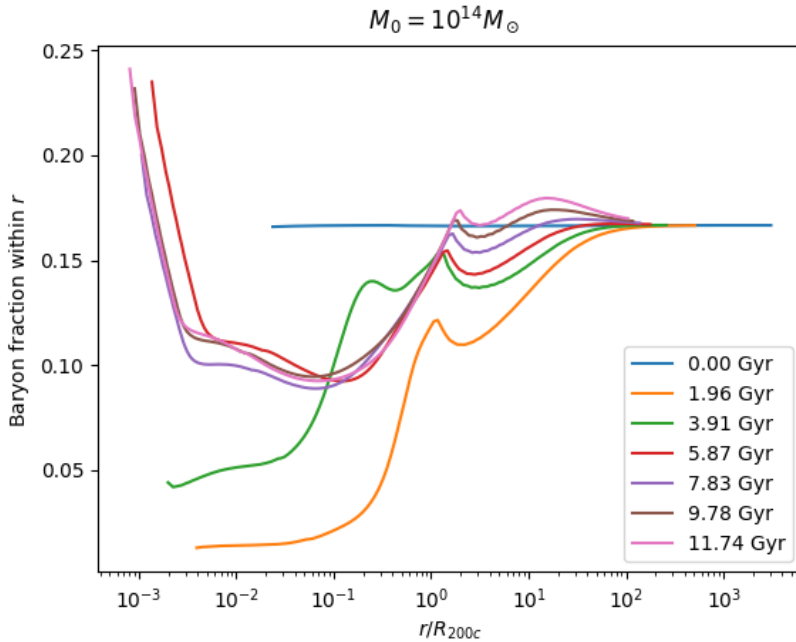


Figure 4.12: Baryon fraction evolution for a cooling flow run with $M_0 = 10^{14} M_\odot$, using the same time-dependent parameters in table 4.2. The regions near the virial radius have a baryon fraction close to the universal value, similar to the non-radiative case. The inner regions have much higher baryon fractions, due to the formation of a density cusp in the presence of cooling.

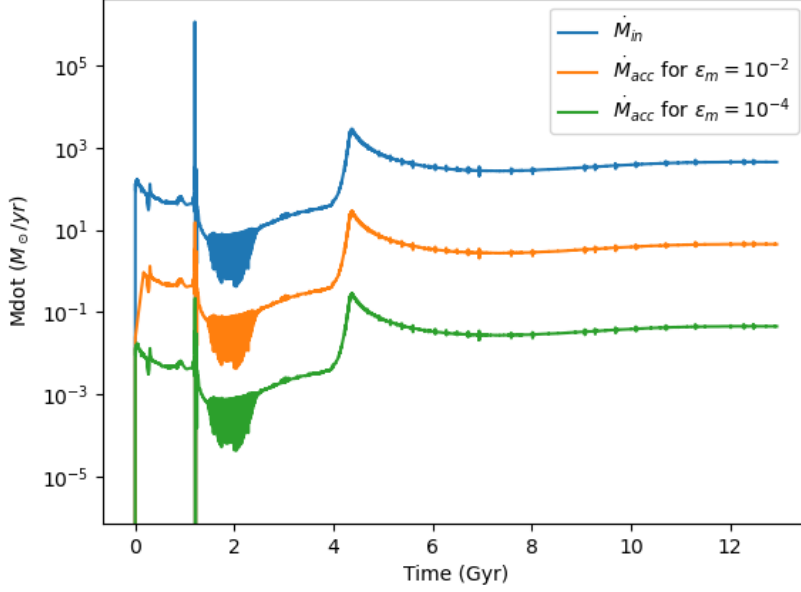


Figure 4.13: Mass infall rate and mass accretion rate for cooling flow run with $M_0 = 10^{14} M_\odot$.

In order to analyze the effect of a cooling flow on the growth of a central black hole, we introduce a seed black hole mass of $M_{BH,0} = 10^6 M_\odot$ and grow its mass by the accretion of cold gas at the center of the halo. We do not input any thermal or mechanical feedback power into the CGM in these runs. Figure 4.13 shows the mass infall rate and the accretion rate for two efficiencies, $\epsilon_m = 10^{-2}$ (corresponding to a total feedback efficiency of 10^{-3}), and $\epsilon_m = 10^{-4}$ (corresponding to a total feedback efficiency of 10^{-5}). We can see that the value of \dot{M}_{acc} is initially limited by the Eddington rate, but after an amount of time t_E (which depends on the value of the efficiency parameters), we have $\dot{M}_{acc} = \epsilon_m \times \dot{M}_{in}$. The larger the feedback efficiency, the longer is t_E (the time taken before the Eddington rate no longer limits the accretion rate).

In figure 4.14, we plot the mass of the central supermassive black hole as a function of time for the two efficiencies as in figure 4.13. The value of M_{BH} is the same for the two cases at early times, as their growth is limited by the Eddington rate. In this phase, $\dot{M}_{acc} = \dot{M}_{Edd} \propto M_{BH}$, so the black hole will grow at an exponential rate, corresponding to the quasar phase of black hole evolution. After this quasar phase, we have $\dot{M}_{acc} \leq \dot{M}_{Edd}$ which leads to a slower growth of the black hole. The accretion rate in this phase is determined by the cooling time of the inner region of the halo and not by the Eddington limit. The plot of M_{BH} vs t eventually flattens out as the value of \dot{M}_{acc} reaches a constant. In the absence of feedback, the value of \dot{M}_{acc} is greater for a greater transport efficiency ϵ_m , so the run with a larger efficiency has a greater final black hole mass.

4.4 Runs with AGN Feedback

In these runs, we introduce AGN jet feedback in our runs with radiative cooling and DK14 parameter evolution. We vary the halo mass, the efficiency, and the seed black hole mass across runs.

The various quantities of interest to us are the cold gas mass within 5 kpc, the mass accretion rate, the jet power, and the minimum value of t_{cool}/t_{ff} over time. The jet power is calculated in a manner similar to [29]. We consider the grids with a temperature greater than a certain threshold value to belong to the bubble/jet material. We then volume-integrate the internal energy density of all cells belonging to the jet to calculate the total power of the jet. As the gas is monoatomic and follows the ideal gas law, the internal energy density is related to the pressure by

$$\rho\epsilon = \frac{P}{\gamma - 1}, \quad (4.11)$$

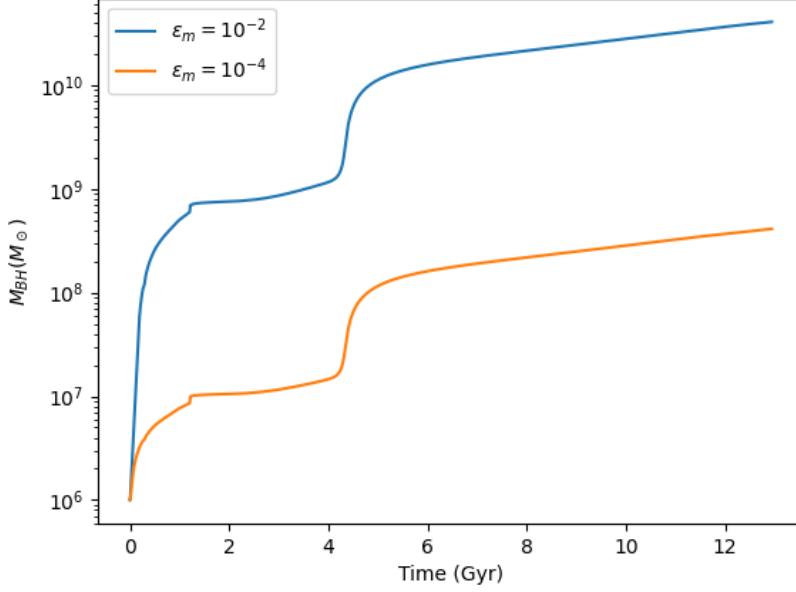


Figure 4.14: Mass of the central SMBH over time for cooling flow run with $M_0 = 10^{14} M_\odot$. The mass of the black holes at $z = 0$ differ by a factor of $\approx 10^2$, which is the same as the difference in mass transport efficiencies ϵ_m . Even though the accretion rate is limited by the Eddington limit at early times, the later stages of evolution mostly depend on the efficiency of mass transport to the event horizon.

where ϵ is the energy per unit mass. The total internal energy is divided by the lifetime of the AGN bubble, which we estimate to be 30 Myr, to obtain the jet power.

The value of $\min(t_{cool}/t_{ff})$ is calculated similar to the cooling flow runs. However, similar to [29], we now only include the warm-hot gas in our calculations ($0.5\text{keV} < T < 8\text{keV}$). The reason for this is that the observations of galaxy clusters is typically done in X-rays, which emit in this temperature range.

4.4.1 General Properties

Figure 4.15 shows the density and temperature of the 2D AGN feedback run in the r-z plane at different times. The total feedback efficiency is 10^{-5} ($\epsilon_{BH} = 0.1$ and $\epsilon_m = 10^{-4}$), the halo mass is $M_0 = 10^{14} M_\odot$, and the seed black hole mass is $M_{BH,0} = 10^6 M_\odot$. At the center of the halo, the density is high and therefore the cooling time is short. The gas is rapidly cooled and flows toward the center, giving rise to a high value of \dot{M}_{in} . This launches the bipolar jets at the center. Although our mathematical and physical implementation of the jets are symmetric, the evolution of the gas is not perfectly symmetric especially at later times, as the evolution of the jets is shaped by the presence of cold gas in their way.

The jet injection process is very fast, but eventually the hot gas slows down and reaches a near pressure balance. The jet quickly "throws out" the central gas and drastically lowers the value of \dot{M}_{in} , preventing the further power injection into the jet. This results in the formation of bubbles which detach from the central region and rise buoyantly. The hot, low dense material of the jet mixes with the ICM, heating up the ICM core and reducing the jet power.

In the absence of continued energy injection from the AGN jet, the multiphase ICM gas begins to cool again. The condensation of the cold gas increases the value of \dot{M}_{acc} and relaunches the AGN jets. Thus, a self-regulating cycle of heating and cooling in the halo core is formed.

In figure 4.16, we plot the cold gas mass within 5 kpc, \dot{M}_{acc} , the normalized jet power, and $\min(t_{cool}/t_{ff})$ as a function of time for the same halo mass. We can clearly see that the values \dot{M}_{acc} , the normalized jet power, and $\min(t_{cool}/t_{ff})$ behave coherently, typically increasing during the heating portion of a cycle and decreasing during the cooling portion of the cycle. Strictly speaking, there is some time lag between an increase in \dot{M}_{acc}

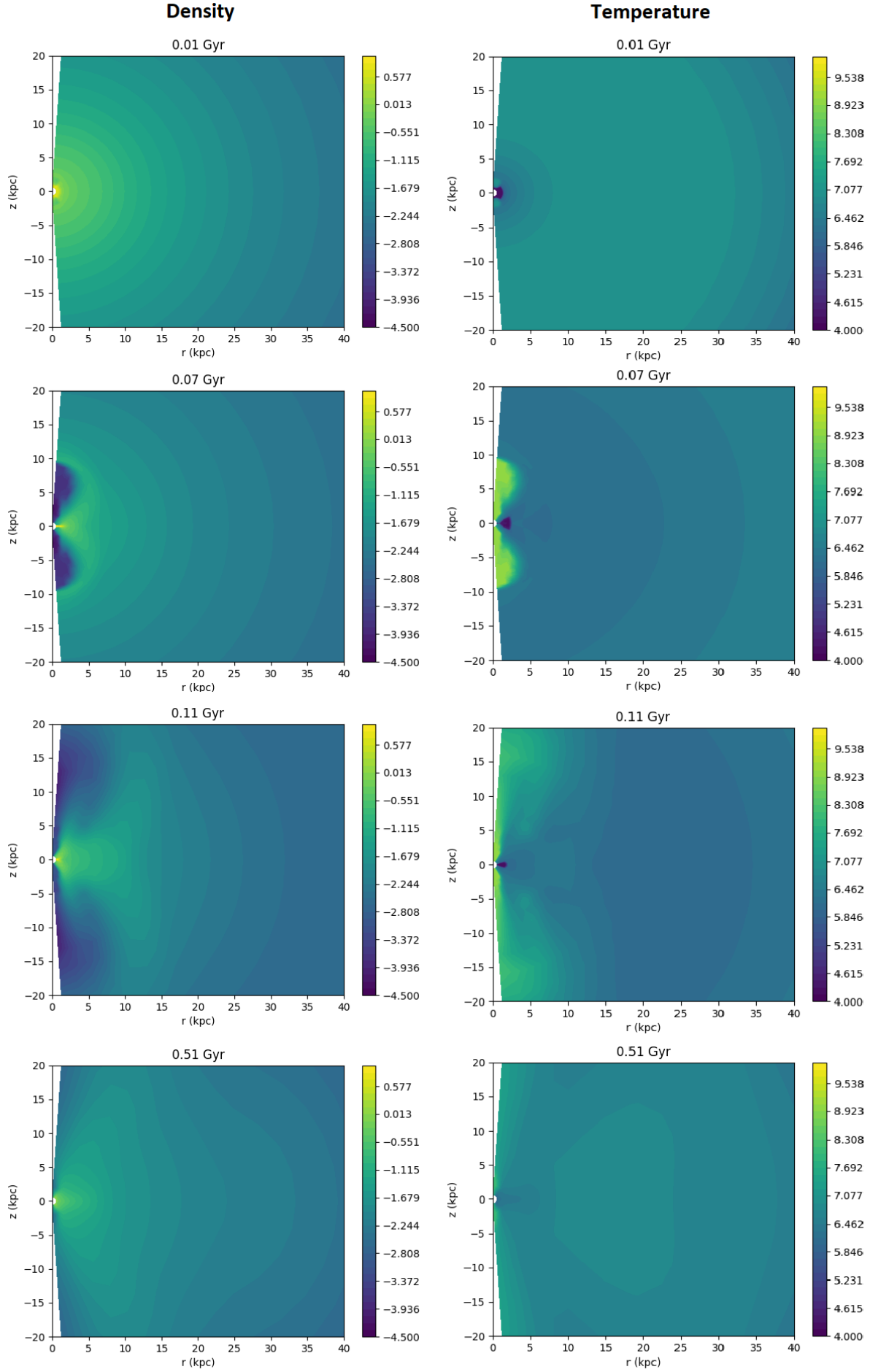


Figure 4.15: Snapshots of the density (left) and temperature (right) for $M_0 = 10^{14} M_\odot$ and $\epsilon_m = 10^{-4}$.

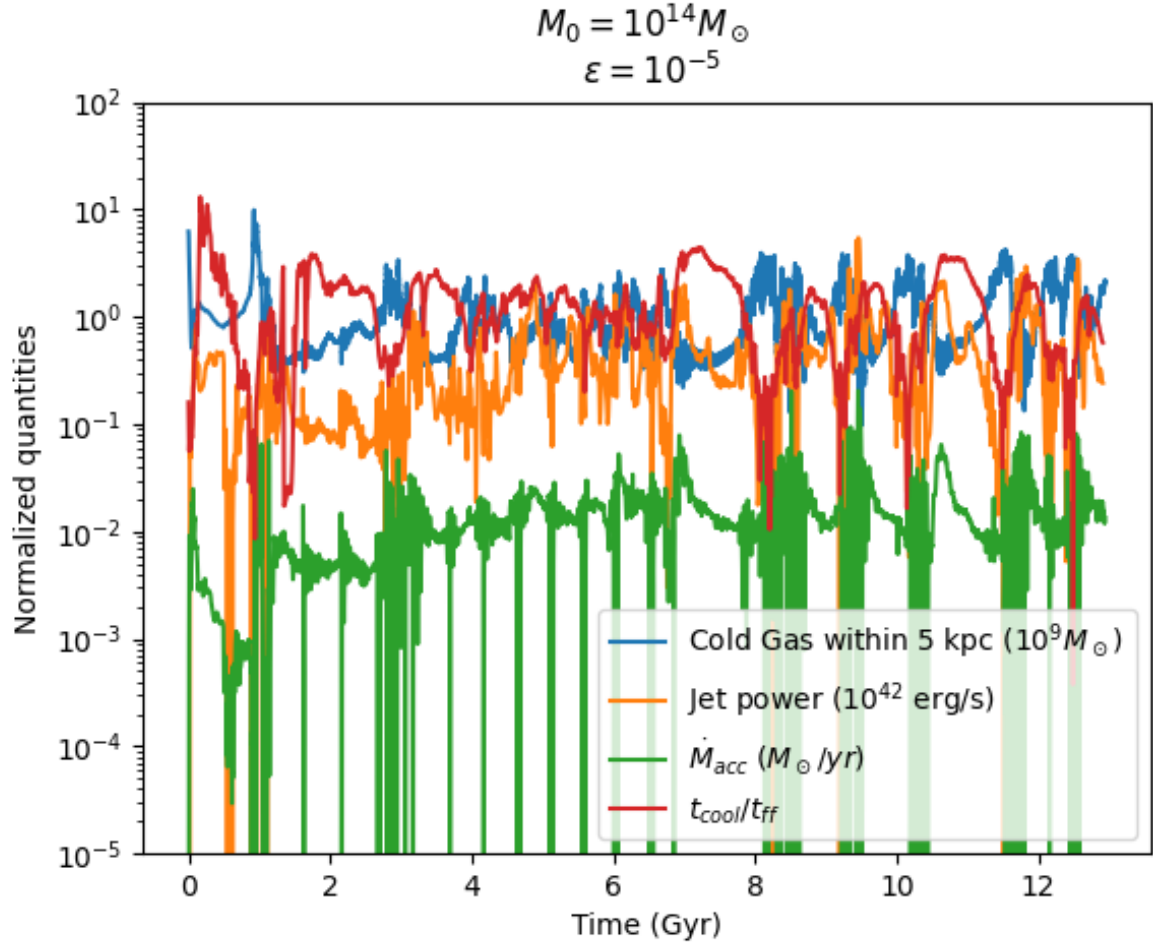


Figure 4.16: Normalized quantities \dot{M}_{acc} , $M_{cold}(< 5\text{kpc})$, jet power (calculated by the method described in section 4.4), and $\min(t_{cool}/t_{ff})$ for $M_0 = 10^{14} M_\odot$, $\epsilon_m = 10^{-4}$, and $M_{BH,0} = 10^6 M_\odot$. The data is sampled every ~ 10 Myr. The spikes in jet power are mostly associated with increase in $\min(t_{cool}/t_{ff})$, increase in black hole accretion rate, and decrease in cold gas mass within 5 kpc, indicating heating and uplifting of gas by the AGN jets.

and an increase in the jet power and $\min(t_{cool}/t_{ff})$, as we first require a high accretion rate in order to launch the AGN jets and heat the gas. However, this time lag is very small (few Myr). The cold gas mass behaves in an opposite manner, decreasing in the heating cycle and increasing in the cooling cycle.

4.4.2 Varying the efficiency

We fix the halo mass as either $10^{14} M_\odot$ or $10^{15} M_\odot$ and the seed black hole mass as $M_{BH,0} = 10^6 M_\odot$. The mass-to-energy conversion efficiency is kept constant at $\epsilon_{BH} = 0.1$, and the mechanical transport efficiency is varied across runs.

In the absence of continued high jet power, the gas cools by radiative cooling and falls toward the center again. The value of \dot{M}_{in} increases again, which can power up the jets. This results in a cycle of cooling and heating of the halo core. The timescale of the cycles depends on the cooling and heating times of the halo core. AGN feedback with a high efficiency results in rapid heating of the gas and the inner material being ejected from the core, requiring a longer time to cool and accrete at the center again. On the other hand, a low feedback efficiency leads to less rapid heating of the gas, and the heated gas does not get completely ejected from the core. This gas can cool and condense in a shorter time. Therefore, the timescale of the AGN cycles is longer for higher efficiencies.

In figure 4.17, we plot the same four quantities as figure 4.16, for various efficiencies and halo masses. We can clearly see that larger efficiencies have larger values of $\min(t_{cool}/t_{ff})$ during the heating phase and that the cycles of cooling and heating are longer. With increase in feedback efficiency, the AGN jet heats up the core

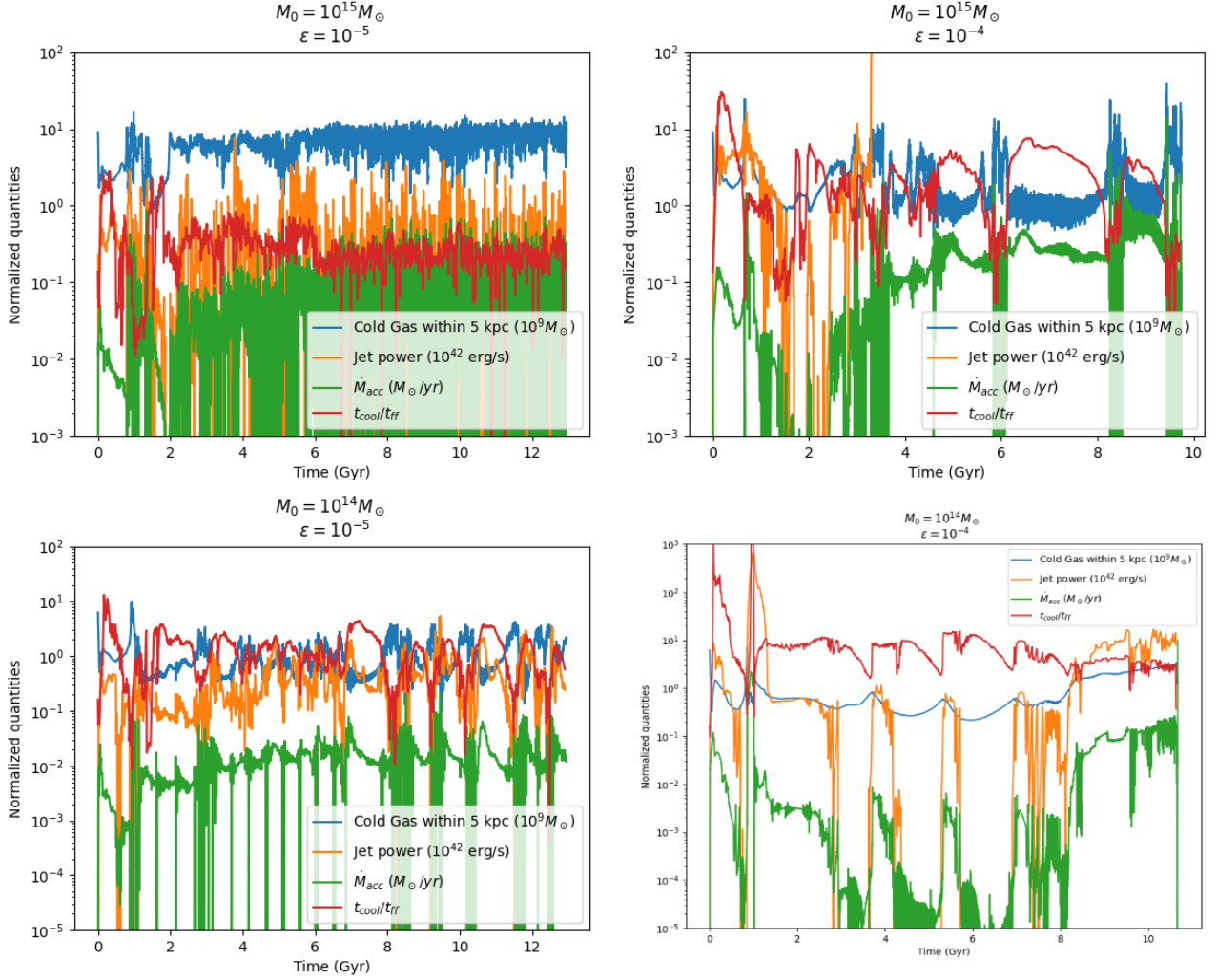


Figure 4.17: Same quantities as figure 4.16 for different efficiencies and halo masses. It is clear that feedback runs with a larger efficiency are characterized by greater jet power, larger values of $\min(t_{\text{cool}}/t_{\text{ff}})$, and longer heating/cooling cycles, indicating that more gas is expelled from the core. Smaller halo masses also show similar results.

and ejects the gas away from the center to a greater degree. This will lead to a decrease in inflowing cold gas at the halo core. In figure 4.18, we plot the average value of \dot{M}_{in} for different efficiencies, normalized to the value corresponding to the cooling flow run (no feedback). The value of \dot{M}_{acc} follows a more complicated trend. The

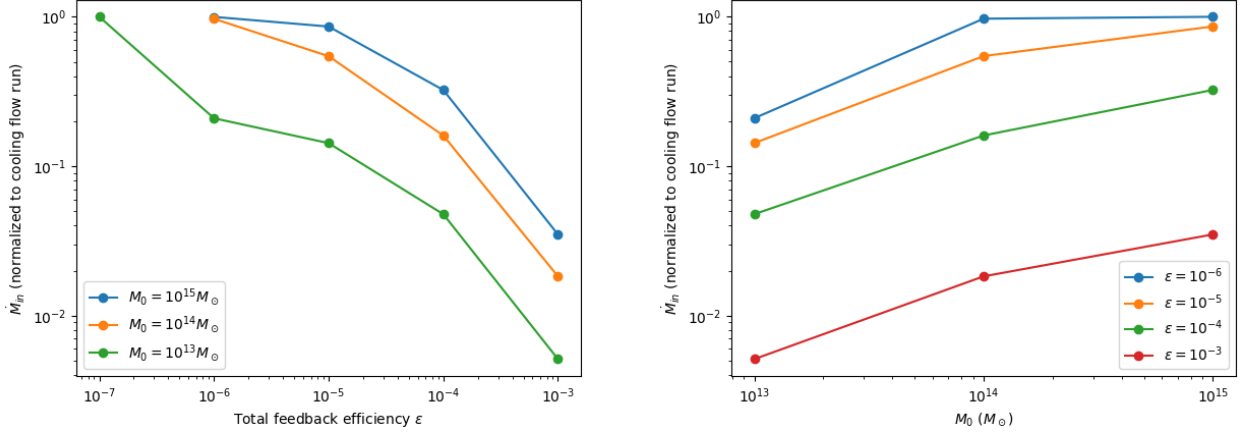


Figure 4.18: Variation of the time-averaged mass inflow rate at ~ 1 kpc with efficiency (left panel) and halo mass (right panel), normalized to the corresponding cooling flow run for each halo. Left: average \dot{M}_{in} vs total efficiency ϵ for different halo masses. Right: average \dot{M}_{in} vs M_0 for different values of ϵ . It is clear that the inflow rate at \dot{M}_{in} is more suppressed for greater efficiency as well as lower halo masses.

accretion rate is related to the mass inflow rate as $\dot{M}_{acc} = \epsilon_m \times \dot{M}_{in}$. For the same value of \dot{M}_{in} , the values of \dot{M}_{acc} increases with mechanical efficiency. Therefore, with increase in ϵ_m , there is a tradeoff between more efficient transport from the inner boundary to the black hole's event horizon, and the decrease in inflowing cold gas at the inner boundary as efficient feedback prevents gas inflow. In figure 4.19 we plot the average \dot{M}_{acc} vs feedback efficiency. We can see that the average \dot{M}_{acc} increases with increase in efficiency, meaning that the increase in accretion rate due to greater transport efficiency to the event horizon more than makes up for the decrease in accretion rate due to the more powerful AGN jets. [29] found that the value of \dot{M}_{in} for a fixed halo mass varies as $\epsilon^{-2/3}$. Since $\dot{M}_{acc} = \epsilon \times \dot{M}_{in}$ (in the radio phase), we expect that it increases with efficiency as $\epsilon^{1/3}$.

4.4.3 Varying the Halo Mass

From figure 4.18, we can see that for the same efficiency, lower mass halos have the mass inflow rate suppressed more. This means that the feedback is more effective for lower mass halos. The same is reflected in figure 4.17, as the runs with $M_0 = 10^{14} M_\odot$ in general have larger values of $\min(t_{cool}/t_{ff})$ compared to the runs with $M_0 = 10^{15} M_\odot$. Thus, the effect of decreasing the halo mass is similar to the effect of increasing the efficiency, similar to the results of [29]. This implies that a larger feedback efficiency is required to suppress the inflow rate to the same degree in a more massive halo.

We note that massive halos have deeper potential wells, and therefore require a greater change in energy in order to change the dynamics of the gas. Therefore in order to disrupt the core to the same degree, a greater efficiency is required in more massive halos compared to less massive halos, which can be easily disrupted.

4.4.4 Varying the Seed Black Hole Mass

In the initial stages of AGN feedback, the mass accretion rate is limited by the Eddington rate of the central SMBH, leading to a quasar phase of AGN evolution. Since $\dot{M}_{Edd} \propto M_{BH}$, the seed black hole mass plays an important role only at early times. In addition, the values of the two efficiencies (mechanical transport efficiency and energy conversion efficiency) also play an important role in the initial evolution of the Eddington rate and the mass of the black hole.

In figure 4.20, we plot the value of $\dot{M}_{acc}/\dot{M}_{Edd}$ for different seed masses and efficiencies. We can see that the first quasar phase, where $\dot{M}_{acc} = \dot{M}_{Edd}$ for a continued duration, lasts longer for smaller seed BH masses, ranging

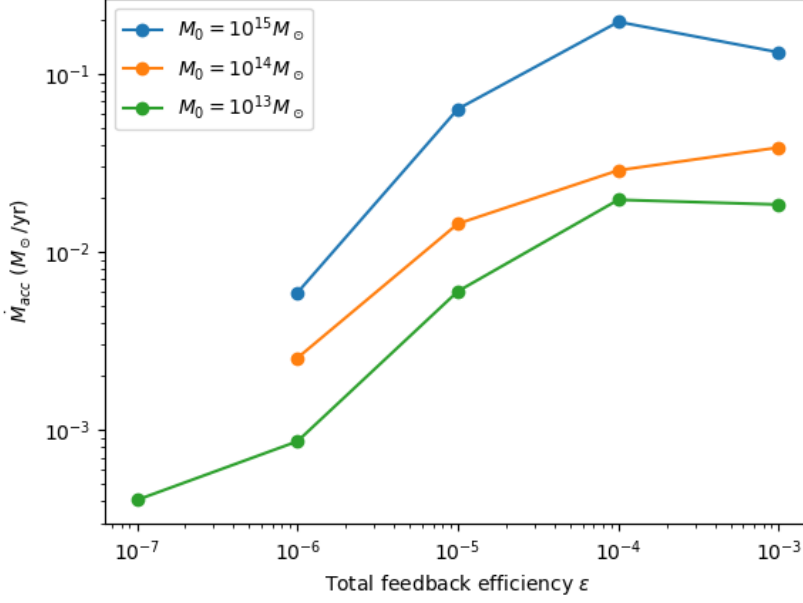


Figure 4.19: Variation of the SMBH accretion rate \dot{M}_{acc} with efficiency. The accretion rate is defined as $\min(\epsilon_m \dot{M}_{in}, \dot{M}_{Edd})$. We can see from the figure that the accretion rate increases with increase in efficiency, as opposed to the inflow rate \dot{M}_{in} . The decrease in inflow rate due to the heating and expulsion of gas from the AGN jets is more than compensated by the increase in the fraction of mass that is transported to the black hole event horizon.

from $\sim 0.2 \text{ Gyr}$ for $M_{BH,0} = 10^4 M_\odot$ to only a few Myr for $M_{BH,0} = 10^7 M_\odot$. In figure 4.21, we plot the mass of

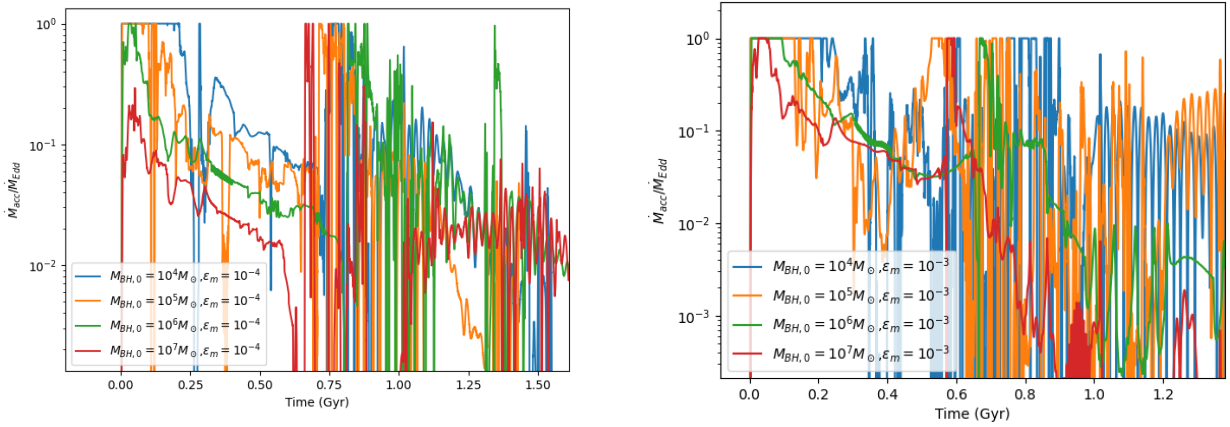


Figure 4.20: Value of $\dot{M}_{acc}/\dot{M}_{Edd}$ over time for different seed black hole masses and efficiencies. The runs with a smaller seed black hole mass have a longer initial time period where $\dot{M}_{acc} \sim \dot{M}_{Edd}$, ranging from $\sim 200 \text{ Myr}$ for $M_{BH,0} = 10^4 M_\odot$ to only a few Myr for $M_{BH,0} = 10^7 M_\odot$.

the black hole as a function of time for different initial conditions and efficiencies. The mass of the black hole at various times for the various cases is tabulated in table 4.3. We can see that even though the initial masses vary by several orders of magnitude, the mass of the black hole after 1 Gyr is largely independent of the seed black hole mass. The masses of the black hole further converge over time. Since the accretion rate is no longer limited by the Eddington limit at later radio stage of AGN evolution, we expect that the evolution of the halo is identical at all later times, regardless of the seed black hole mass. Therefore, we conclude that the feedback efficiency plays a much more important role in the long-term evolution of the halo core and the AGN than the seed black hole mass.

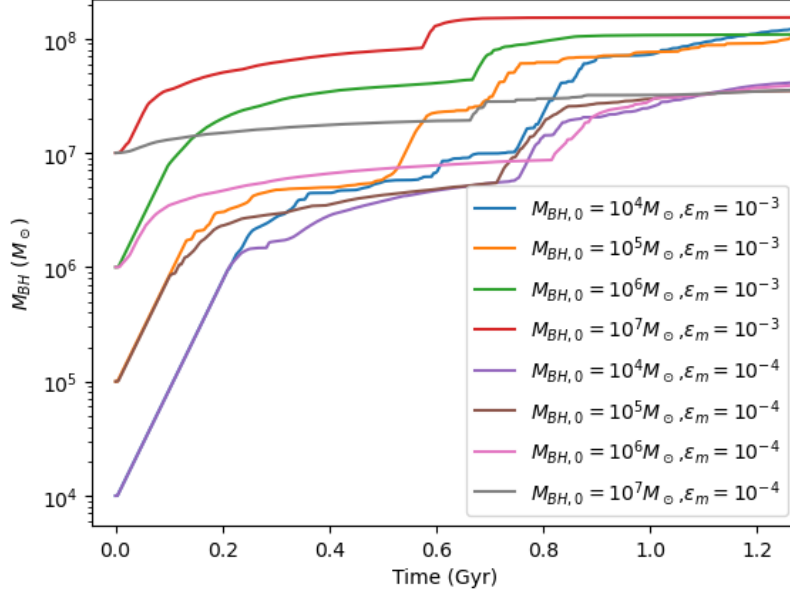


Figure 4.21: Growth of the central SMBH for different seed black hole masses and efficiencies. The black holes grow exponentially with time in the initial quasar stage of evolution (corresponding to the linear portion of the semilog graph). It is clear that after the initial growth phase, the value of $M_{BH,0}$ is largely independent of the initial mass, and the value of ϵ_m plays a much more important role in the evolution at later stages.

Table 4.3: Mass of the black hole at various stages of the AGN evolution.

$M_{BH,0}$	ϵ_m	$M_{BH}(0.5 \text{ Gyr})$	$M_{BH}(1 \text{ Gyr})$
$10^4 M_\odot$	10^{-4}	$3.81 \times 10^6 M_\odot$	$2.48 \times 10^7 M_\odot$
$10^5 M_\odot$	10^{-4}	$4.28 \times 10^6 M_\odot$	$2.97 \times 10^7 M_\odot$
$10^6 M_\odot$	10^{-4}	$7.27 \times 10^6 M_\odot$	$2.86 \times 10^7 M_\odot$
$10^7 M_\odot$	10^{-4}	$1.84 \times 10^7 M_\odot$	$3.20 \times 10^7 M_\odot$
$10^4 M_\odot$	10^{-3}	$5.56 \times 10^6 M_\odot$	$7.21 \times 10^7 M_\odot$
$10^5 M_\odot$	10^{-3}	$5.84 \times 10^6 M_\odot$	$7.60 \times 10^7 M_\odot$
$10^6 M_\odot$	10^{-3}	$3.78 \times 10^7 M_\odot$	$1.07 \times 10^8 M_\odot$
$10^7 M_\odot$	10^{-3}	$7.84 \times 10^7 M_\odot$	$1.53 \times 10^8 M_\odot$

4.4.5 Baryon Fraction Evolution

The feedback process introduces AGN bubbles in the inner regions of the halo, severely decreasing the average density compared to the adiabatic and cooling flow runs. Therefore, the baryon fraction in the inner regions of the halo is much smaller than with non-radiative and cooling flows. Figure 4.22 shows the baryon fraction as a function of radius for our feedback runs. To visualize the variation in the innermost regions better, the y-axis is also log-scaled. We can see that the value of f_b within $\sim 10^{-2} R_{200c}$ is at least an order of magnitude lesser than the universal value.

It is also clear from figure 4.22 that the feedback affects the baryon fraction of only the innermost regions of the halo, as the value of f_b outside of $\sim 10^{-1} R_{200c}$ is very similar to the adiabatic and cooling flow cases. Using the density parameter evolution as in table 4.2, the baryon fraction can be made to reach the universal value near and outside of the virial radius.

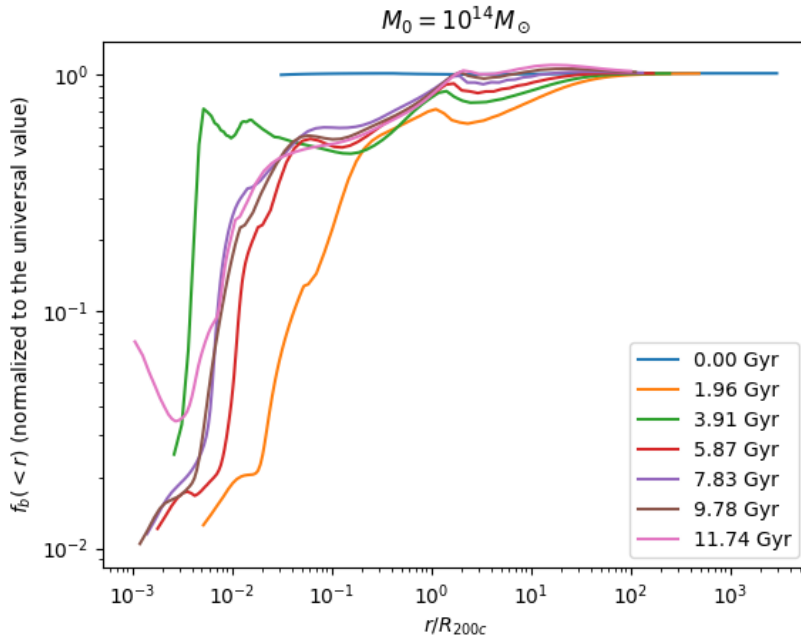


Figure 4.22: Normalized baryon fraction evolution for $M_0 = 10^{14} M_\odot$, with AGN feedback efficiency $\epsilon = 10^{-5}$ and redshift-dependent DK14 parameters (table 4.2). Similar to the effect of radiative cooling, the effects of AGN feedback are prominent only in the inner radii of the halo. The baryon fraction within $10^{-2} R_{200c}$ is very low because the AGN jets cause bubbles with hot, low density gas. The baryon fraction beyond the virial radius reaches the universal value, similar to the non-radiative and cooling flow runs.

Chapter 5

Conclusions

We have studied the evolution of baryonic gas in an isolated dark matter halo. We have modeled most of the physical mechanisms that occurs inside a dark matter halo, including cosmological growth of the halo, Hubble expansion, radiative cooling, AGN jet feedback, and the initial quasar mode of black hole feedback. A major part of halo dynamics that we have yet to model is halo mergers. This is outside the scope of our current work, but we wish to analyze the effect of discrete mergers in a future study. We have implemented a model that is consistent with the cosmological evolution of baryons across halo masses. We also include a self-consistent evolution of the IGM metallicity and growth of the central supermassive black hole.

As opposed to other studies that use a single NFW profile to characterize the halo, we use a profile that transitions from the NFW profile in the inner regions to a more realistic profile in the other regions ([9]). The density profile flattens out to reach the IGM density at large radii. We initialize the gas density as 0.2 (the universal baryon fraction) times the dark matter density. In order to model the effects of Hubble expansion at the outer regions beyond the halo, we introduce a cosmological potential that ensures that gas away from the halo follows Hubble expansion, i.e. $v(r) = H(z)r$.

In the absence of radiative cooling and feedback, the density profiles of the gas behave self-similarly after the initial transient phases. The density profiles show the formation of a core with a nearly constant temperature that depends on the halo mass. The virial shock is formed very early in the run, typically before ~ 1.5 Gyr. Using redshift-dependent parameters to characterize the outer density profile, we show that the baryon fraction at the virial radius reaches within $\sim 15\%$ of the universal baryon fraction at all times.

Radiative cooling in low-mass halos ($M_0 \lesssim 10^{12} M_\odot$) leads to catastrophic cooling within the halo, and no virial shock or density/temperature profile is formed. On the other hand, for high-mass halos, the effects of radiative cooling are prominent only in the inner regions. The density profile is cusp-like in the presence of cooling, which significantly increases the baryon fraction in the inner regions. The gas at radii $> 0.1 R_{200c}$ behave similar to the non-radiative runs, and the baryon fraction reaches the universal value at the virial radius.

The presence of AGN feedback leads to cooling and heating cycles in the halo core, similar to the results of [29]. However, we find that the cycles in our runs are longer than theirs. This can be due to the growth of the halo and the metallicity evolution, which strongly influence the free-fall and cooling times in the halo core. Typically, the heating portion of the feedback cycle is characterized by greater jet power, enhanced accretion onto the central SMBH, and decrease in the cold gas mass in the inner regions. This is also reflected by an increase in $\min(t_{\text{cool}}/t_{\text{ff}})$. A greater feedback efficiency and a smaller halo mass both lead to stronger feedback events and a decrease in mass inflow rate at ~ 1 kpc. On the other hand, the gas accretion onto the SMBH increases with efficiency of mass transport from ~ 1 kpc to the black hole event horizon. For $M_0 = 10^{14} M_\odot$, we find that an efficiency of $\epsilon \sim 10^{-4}$ (relative to the mass inflow rate measured at 1 kpc) suppresses the mass inflow rate by a factor of 10 compared to the cooling flow run, which is consistent with observations.

The growth of the central SMBH can be divided into two regimes: a quasar period where the accretion rate is high ($\dot{M}_{\text{acc}} \sim \dot{M}_{\text{Edd}}$) and a radio period where the accretion rate is low ($\dot{M}_{\text{acc}} \ll \dot{M}_{\text{Edd}}$). We find that the duration of the quasar period primarily depends on the seed black hole mass and the efficiencies of mass transport

to the event horizon, and lasts for $1 - 100$ Myr. This period is characterized by an exponential growth in the black hole mass. At later stages, the black hole growth is slowed down and is mostly independent of the seed black hole mass. The halo mass and mass transport efficiency play a more important role in the further evolution of the AGN.

Our framework for studying gas in an isolated dark matter halo leads to results that are consistent with previous studies, and extends them to higher redshifts. A middle ground between full cosmological simulations and idealized boxes, we hope that our model will lead to new explorations in the field of galaxy formation and evolution.

References

- [1] Yuval Birnboim and Avishai Dekel. Virial shocks in galactic haloes? *Monthly Notices of the Royal Astronomical Society*, 345:349–364, 2003. [1](#), [18](#), [22](#), [23](#)
- [2] H. Böhringer, K. Matsushita, E. Churazov, Y. Ikebe, and Y. Chen. *Astronomy & Astrophysics*, 382:804–820, 2002. [8](#)
- [3] Frank C. van den Bosch, Fangzhou Jiang, Andrew Hearin, Duncan Campbell, Douglas Watson, and Nikhil Padmanabhan. *Monthly Notices of the Royal Astronomical Society*, 445:1713–1730, 2014. [v](#), [5](#), [10](#), [11](#)
- [4] Prakriti Pal Choudhury, Guinevere Kauffmann, and Prateek Sharma. *Monthly Notices of the Royal Astronomical Society*, 485:3430–3445, 2019. [1](#), [17](#), [23](#)
- [5] E. Churazov, S. Sazonov, R. Sunyaev, W. Forman, C. Jones, and H. Böhringer. Supermassive Black Holes in Elliptical Galaxies: Switching from Very Bright to Very Dim. In B. Aschenbach, V. Burwitz, G. Hasinger, and B. Leibundgut, editors, *Relativistic Astrophysics Legacy and Cosmology - Einstein's Legacy*, page 295, 2007. [2](#), [8](#)
- [6] Camila A. Correa, J. Stuart B. Wyithe, Joop Schaye, and Alan R. Duffy. *Monthly Notices of the Royal Astronomical Society*, 450:1514–1520, 2015. [5](#)
- [7] Camila A. Correa, J. Stuart B. Wyithe, Joop Schaye, and Alan R. Duffy. *Monthly Notices of the Royal Astronomical Society*, 450:1521–1537, 2015. [5](#)
- [8] Robert A. Crain, Vincent R. Eke, Carlos S. Frenk, Adrian Jenkins, Ian G. McCarthy, Julio F. Navarro, and Frazer R. Pearce. *Monthly Notices of the Royal Astronomical Society*, 377:41–49, 2007. [21](#)
- [9] Benedikt Diemer and Andrey V. Kravtsov. *The Astrophysical Journal*, 789:1, 2014. [1](#), [6](#), [35](#)
- [10] Alan R. Duffy, Joop Schaye, Scott T. Kay, Claudio Dalla Vecchia, Richard A. Battye, and C. M. Booth. *Monthly Notices of the Royal Astronomical Society*, 405:2161–2178, 2010. [21](#)
- [11] Drummond Fielding, Eliot Quataert, Michael McCourt, and Todd A. Thompson. The impact of star formation feedback on the circumgalactic medium. *Monthly Notices of the Royal Astronomical Society*, 466:3810–3826, 2017. [1](#)
- [12] M. Gaspari, M. Ruszkowski, and P. Sharma. *The Astrophysical Journal*, 746:94, 2012. [8](#)
- [13] Anthony H. Gonzalez, Suresh Sivanandam, Ann I. Zabludoff, and Dennis Zaritsky. *The Astrophysical Journal*, 778:14, 2013. [21](#)
- [14] F. van den Bosch & S. White. H. Mo. *Galaxy Formation and Evolution*. Cambridge University Press, 2011. [4](#), [5](#)
- [15] Philip F. Hopkins, Andrew Wetzel, Dušan Kereš, Claude-André Faucher-Giguère, Eliot Quataert, Michael Boylan-Kolchin, Norman Murray, Christopher C. Hayward, Shea Garrison-Kimmel, Cameron Hummels, Robert Feldmann, Paul Torrey, Xiangcheng Ma, Daniel Anglés-Alcázar, Kung-Yi Su, Matthew Orr, Denise

- Schmitz, Ivanna Escala, Robyn Sanderson, Michael Y. Grudić, Zachary Hafen, Ji-Hoon Kim, Alex Fitts, James S. Bullock, Coral Wheeler, T. K. Chan, Oliver D. Elbert, and Desika Narayanan. *Monthly Notices of the Royal Astronomical Society*, 480:800–863, 2018. [23](#)
- [16] Einasto J. *Trudy Inst. Astroz. Alma-Ata*, 57:87, 1965. [6](#)
- [17] Fangzhou Jiang and Frank C. van den Bosch. *Monthly Notices of the Royal Astronomical Society*, 440(1): 193–207, 2014. [5](#)
- [18] P. A. Knight and T. J. Ponman. *Monthly Notices of the Royal Astronomical Society*, 289:955–972, 1997. [22](#)
- [19] Andrey V. Kravtsov, Daisuke Nagai, and Alexey A. Vikhlinin. *The Astrophysical Journal*, 625:588–598, 2005. [21](#)
- [20] Amandine M. C. Le Brun, Ian G. McCarthy, Joop Schaye, and Trevor J. Ponman. *Monthly Notices of the Royal Astronomical Society*, 441:1270–1290, 2014. [21](#)
- [21] James McBride, Onsi Fakhouri, and Chung-Pei Ma. *Monthly Notices of the Royal Astronomical Society*, 398:1858–1868, 2009. [5](#)
- [22] A. Mignone, G. Bodo, S. Massaglia, T. Matsakos, O. Tesileanu, C. Zanni, and A. Ferrari. *The Astrophysical Journal Supplement Series*, 170:228–242, 2007. [10](#)
- [23] Brian R. McNamara Myriam Gitti, Fabrizio Brighenti. *Advances in Astronomy*, 2012, 2012. [8](#)
- [24] B. B. Nath and N. Trentham. *Monthly Notices of the Royal Astronomical Society*, 291:505–516, 1997. [7](#), [14](#)
- [25] White S. D. M. Navarro J. F., Frenk C. S. *The Astrophysical Journal*, 462:563, 1996. [1](#), [6](#)
- [26] Benjamin D. Oppenheimer and Romeel Davé. *Monthly Notices of the Royal Astronomical Society*, 373: 1265–1292, 2006. [7](#), [14](#)
- [27] Molly S. Peeples, Jessica K. Werk, Jason Tumlinson, Benjamin D. Oppenheimer, J. Xavier Prochaska, Neal Katz, and David H. Weinberg. *The Astrophysical Journal*, 786:54, 2014. [7](#)
- [28] S. Planelles, S. Borgani, G. Murante, L. Tornatore, K. Dolag, and D. Fabjan. Baryon census in hydrodynamical simulations of galaxy clusters. In J. C. Guirado, L. M. Lara, V. Quilis, and J. Gorgas, editors, *Highlights of Spanish Astrophysics VII*, pages 457–457, 2013. [21](#)
- [29] Deovrat Prasad, Prateek Sharma, and Arif Babul. *The Astrophysical Journal*, 811:108, 2015. [1](#), [8](#), [16](#), [26](#), [27](#), [31](#), [35](#)
- [30] Deovrat Prasad, Prateek Sharma, and Arif Babul. *The Astrophysical Journal*, 863:62, 2018. [8](#)
- [31] Schechter P. Press W. H. *The Astrophysical Journal*, 187:425, 1974. [5](#)
- [32] Emilio Romano-Díaz, Enrico Garaldi, Mikolaj Borzyszkowski, and Cristiano Porciani. *Monthly Notices of the Royal Astronomical Society*, 469:1809–1823, 2017. [21](#)
- [33] R. Sadat and A. Blanchard. *Astronomy and Astrophysics*, 371:19–24, 2001. [21](#)
- [34] K. M. Schure, D. Kosenko, J. S. Kaastra, R. Keppens, and J. Vink. *Astronomy & Astrophysics*, 508:751–757, 2009. [7](#)
- [35] Prateek Sharma, Michael McCourt, Eliot Quataert, and Ian J. Parrish. *Monthly Notices of the Royal Astronomical Society*, 420:3174–3194, 2012. [8](#)
- [36] S. Shen, J. Wadsley, and G. Stinson. *Monthly Notices of the Royal Astronomical Society*, 407:1581–1596, 2010. [7](#)

- [37] Debora Sijacki, Volker Springel, Tiziana Di Matteo, and Lars Hernquist. *Monthly Notices of the Royal Astronomical Society*, 380:877–900, 2007. [2](#), [8](#)
- [38] D. N. Spergel, R. Bean, O. Doré, M. R. Nolta, C. L. Bennett, J. Dunkley, G. Hinshaw, N. Jarosik, E. Komatsu, L. Page, H. V. Peiris, L. Verde, M. Halpern, R. S. Hill, A. Kogut, M. Limon, S. S. Meyer, N. Odegard, G. S. Tucker, J. L. Weiland, E. Wollack, and E. L. Wright. *The Astrophysical Journal Supplement Series*, 170:377–408, 2007. [1](#), [4](#)
- [39] Volker Springel, Rüdiger Pakmor, Annalisa Pillepich, Rainer Weinberger, Dylan Nelson, Lars Hernquist, Mark Vogelsberger, Shy Genel, Paul Torrey, Federico Marinacci, and Jill Naiman. *Monthly Notices of the Royal Astronomical Society*, 475:676–698, 2018. [1](#)
- [40] Jonathan Stern, Amiel Sternberg, Claude-André Faucher-Giguère, Zachary Hafen, Drummond Fielding, Eliot Quataert, Andrew Wetzel, Daniel Anglés-Alcázar, Kareem El-Badry, Dušan Kereš, and Philip F. Hopkins. [23](#)
- [41] Frank C. van den Bosch. *Monthly Notices of the Royal Astronomical Society*, 331:98–110, 2002. [5](#)
- [42] Ye Wang, G. J. Ferland, M. L. Lykins, R. L. Porter, P. A. M. van Hoof, and R. J. R. Williams. *Monthly Notices of the Royal Astronomical Society*, 440:3100–3112, 2014. [7](#)
- [43] Steven Weinberg. *Gravitation and Cosmology: Principles and Applications of the General Theory of Relativity*. 1972. [3](#)
- [44] Robert P. C. Wiersma, Joop Schaye, and Britton D. Smith. *Monthly Notices of the Royal Astronomical Society*, 393:99–107, 2009. [v](#), [7](#), [14](#), [15](#)
- [45] Robert P. C. Wiersma, Joop Schaye, Tom Theuns, Claudio Dalla Vecchia, and Luca Tornatore. *Monthly Notices of the Royal Astronomical Society*, 399:574–600, 2009. [7](#), [14](#)
- [46] H. Y. Karen Yang and Christopher S. Reynolds. *The Astrophysical Journal*, 829:90, 2016. [8](#)
- [47] D. H. Zhao, Y. P. Jing, H. J. Mo, and G. Börner. *The Astrophysical Journal*, 707:354–369, 2009. [6](#), [11](#)